AGU PUBLICATIONS

Paleoceanography

RESEARCH ARTICLE
10.1002/2014PA002734

Key Points:
- Oligocene-Miocene magnetobiostratigraphic chronology
- Changes in planktonic productivity during the Mi-1 glacial event
- Transient variations in SW Atlantic bottom water flow patterns

Correspondence to:
F. Florindo,
fabio.florindo@ingv.it

Citation:
Florindo, F., R. Gennari, D. Persico, E. Turco, G. Villa, P. C. Lurcock, A. P. Roberts, A. Winkler, L. Carter, and S. F. Pekar (2015), New magnetobiostratigraphic chronology and paleoceanographic changes across the Oligocene-Miocene boundary at DSDP Site 516 (Rio Grande Rise, SW Atlantic), *Paleoceanography*, *30*, 659–681, doi:10.1002/2014PA002734.

Received 6 OCT 2014
Accepted 15 MAY 2015
Accepted article online 19 MAY 2015
Published online 11 JUN 2015

New magnetobiostratigraphic chronology and paleoceanographic changes across the Oligocene-Miocene boundary at DSDP Site 516 (Rio Grande Rise, SW Atlantic)

Fabio Florindo[1], Rocco Gennari[2], Davide Persico[2], Elena Turco[2], Giuliana Villa[2], Pontus C. Lurcock[1], Andrew P. Roberts[3], Aldo Winkler[1], Lionel Carter[4], and Stephen F. Pekar[5,6]

[1]Istituto Nazionale di Geofisica e Vulcanologia, Rome, Italy, [2]Dipartimento di Fisica e Scienze della Terra, Università di Parma, Parma, Italy, [3]Research School of Earth Sciences, The Australian National University, Canberra, Australia, [4]Antarctic Research Centre, Victoria University of Wellington, Wellington, New Zealand, [5]School of Earth and Environmental Sciences, Queens College, Flushing, New York, USA, [6]Lamont-Doherty Earth Observatory, Columbia University, New York, New York, USA

Abstract New magnetobiostratigraphic data for the late Oligocene through early Miocene at Deep Sea Drilling Project (DSDP) Hole 516F provide a significantly revised age model, which permits reevaluation of developments that led to the Mi-1 glacial event at the Oligocene-Miocene boundary. Our new high-resolution paleomagnetic study, which is supported by quantitative calcareous nannofossil and planktonic foraminiferal analyses, significantly refines previous age models for Oligocene-Miocene sediments from DSDP Hole 516F, with ages that are systematically younger than those previously determined. In some parts of the Oligocene, the discrepancy with previous studies exceeds 450 kyr. Based on this new age model, we infer a progressive increase in sedimentation rate and paleoproductivity between circa 23.9 Ma and circa 22.9 Ma, with the highest rate coinciding with the Mi-1 glacial event at the Oligocene-Miocene boundary. This productivity increase would have resulted in higher rates of carbon burial and in turn a drawdown of atmospheric CO_2. Immediately afterward, an abrupt decrease in sedimentation rate and paleoproductivity suggests that the Mi-1 deglaciation was associated with decreased carbon input into the ocean. Elevated sedimentation rates are also documented at ~24.5 Ma, coincident with the Oi2D glacioeustatic event. The presence of volcanic material within the sediments during these glacial events is interpreted to have resulted from redeposition of sediment scoured from nearby sites on the Rio Grande Rise due to transient variations in bottom water flow patterns.

1. Introduction

Transient and long-term oceanographic and climatic changes occurred during the late Oligocene to early Miocene [e.g., *Wright et al.*, 1991; *Zachos et al.*, 1992; *Pekar and DeConto*, 2006; *Pekar et al.*, 2006; *Wilson et al.*, 2009, and references therein] whose mechanisms and extents remain unresolved. Late Oligocene warming [e.g., *Villa and Persico*, 2006] is evident from a large decrease (~1‰) in global composite $\delta^{18}O$ records, which is interpreted to have resulted from bottom water warming, although any decrease in Antarctic ice volume is still uncertain, ranging from a collapse of an Antarctic ice sheet (AIS) to an ice sheet that ranged from 50 up to 100% of the current ice sheet volume [*Pekar et al.*, 2006]. In addition, intensification of the Antarctic Circumpolar Current (ACC) in the late Oligocene [e.g., *Pekar et al.*, 2006; *Barker et al.*, 2007; *Lyle et al.*, 2007] produced extensive sedimentary deep-sea hiatuses in the Southern Ocean [e.g., *Woodruff and Savin*, 1989; *Wright et al.*, 1991; *Roberts et al.*, 2003a; *Florindo and Roberts*, 2005] and surface water cooling [e.g., *Billups et al.*, 2002; *Lyle et al.*, 2007] which may have also affected global ocean circulation patterns.

The Mi-1 deep-sea oxygen isotope event at the Oligocene-Miocene boundary (23.03 Ma, base of subchron C6Cn.2n) [*Gradstein et al.*, 2012] has been interpreted to represent a significant, albeit transient, increase in continental ice volume [e.g., *Naish et al.*, 2001; *Roberts et al.*, 2003b; *Pekar et al.*, 2006; *Wilson et al.*, 2009; *Liebrand et al.*, 2011; *Mawbey and Lear*, 2013] and bottom water cooling [e.g., *Billups and Schrag*, 2002; *Pekar et al.*, 2002]. While the causal mechanism of the Mi-1 event has been ascribed to low variance in orbital eccentricity combined with low-amplitude obliquity variability [*Zachos et al.*, 2001a, 2001b] and while "cooling of deep-ocean waters may have played a role in triggering" this event [*Shevenell and Kennett*, 2007], circulation changes in the Southern Ocean are still poorly understood due to extensive

regional hiatuses across this event. These hiatuses extend into the early Miocene, which hinders understanding of Southern Ocean paleocirculation for this time interval. Recent evidence from the latest Oligocene indicates that higher-productivity conditions occurred in the Atlantic basin, which would have led to higher rates of carbon burial, and suggests a link between carbon cycling and climate changes [*Diester-Haass et al.*, 2011; *Mawbey and Lear*, 2013]. However, the areal extent and timing of this increase is not well constrained.

Site 516 was cored in March 1980 during Deep Sea Drilling Project (DSDP) Leg 72 (Southwest Atlantic), which aimed to improve understanding of the origin and subsidence history of the Rio Grande Rise, an important component of any model for South Atlantic paleoceanographic development [e.g., *Barker et al.*, 1981, 1983]. This bathymetric feature intersects several major southwestern Atlantic water masses and plays an important role in controlling deep and intermediate ocean circulation (Figure 1).

Magnetostratigraphic results from DSDP Hole 516F were included in the overall site chronology produced by *Berggren et al.* [1983]. Despite the low sampling resolution (approximately 1 sample/3 m for paleomagnetic and biostratigraphic analyses), a set of biostratigraphic events was subsequently calibrated to the DSDP Hole 516F magnetostratigraphy [e.g., *Berggren et al.*, 1983, 1985, 1995; *Spezzaferri*, 1994]. This site has become the focus of several later paleoceanographic and paleoclimatic studies [e.g., *Hess et al.*, 1986; *Miller et al.*, 1988; *Pagani et al.*, 2000, 2005; *Henderiks and Pagani*, 2007; *Plancq et al.*, 2012, 2013] because of its relatively continuous pelagic sedimentation, its position above the lysocline and the calcite compensation depth (CCD) during the Miocene, and its bathymetric isolation from terrigenous sediment sources. Unfortunately, the conclusions of these studies rest upon the low-resolution age model of *Berggren et al.* [1983]. This situation prompted us to reinvestigate the magnetobiostratigraphy of this site by conducting new high-resolution sampling for paleomagnetic and quantitative calcareous nannofossil and planktonic foraminiferal analyses. Here we present a new age model for the upper Oligocene to lowest Miocene section from Hole 516F. The integrated high-resolution calcareous plankton biostratigraphy is presented by *Gennari et al.* [2014]. In addition to the need for a revised chronology, ongoing debate exists as to whether the present water mass distribution and circulation patterns at different depths in the southwestern Atlantic Ocean are comparable with the overall flow structure at the Oligocene-Miocene boundary. *Dalziel et al.* [2013] suggested that a now-submerged remnant volcanic arc in the central Scotia Sea may have formed a barrier to deep eastward oceanic circulation from the Pacific to the Atlantic Ocean until the late Miocene. In this scenario, southwestern Atlantic circulation before the late Miocene would have been less intense, with minimal bottom water formation and perhaps a weak and simple N-S overturning circulation. Here we present an analysis of sedimentary magnetic properties that contributes to this discussion.

2. Site Location and Lithology

During DSDP Leg 72, seven holes were cored by the D/V *Glomar Challenger* at Site 516 near the crest of Rio Grande Rise (30°16′S, 35°17′W; water depth 1313 m), a prominent bathymetric feature in the South Atlantic basin with more than 4000 m of relief (Figure 1). The rise is part of the Rio Grande-Walvis system, which formed in the Late Cretaceous at or near the mid-ocean ridge crest as an oceanic island and has subsided steadily ever since [e.g., *Barker et al.*, 1981, 1983; *Barker*, 1983; *O'Connor and Duncan*, 1990; *Mohriak et al.*, 2010].

Hole 516F was washed to 169.1 m, then rotary drilled to a depth of 1270.6 m (core 128, in basalts) below the mudline, with an average core recovery of 63%. It was the shallowest site drilled during Leg 72, and sediments representative of the shallow and intermediate southwest Atlantic water masses were cored (Figure 1). The sediments, which become progressively more lithified downsection, are predominantly biogenic (calcareous with a small siliceous component). The upper Oligocene to lower Miocene portion of the record, which was studied here, contains two main lithostratigraphic units. Lithostratigraphic Unit 1 consists of poorly consolidated calcareous ooze that spans cores 1 to 3, from 169.1 to 193 m below sea floor (m bsf), and was deposited well above the CCD: *Barker* [1983] estimated a site paleodepth of 900 m at the Oligocene-Miocene boundary. Principal constituents of Unit 1 are calcareous nannofossils and planktonic foraminifera, with total carbonate content averaging 90%. Unit 2 spans cores 3 to 18, from 193 to 332 m bsf, and consists of nannofossil and foraminiferal chalks with chert nodules and biogenic silica. Carbonate contents range from 75 to 90%; nannofossils make up the main biogenic component.

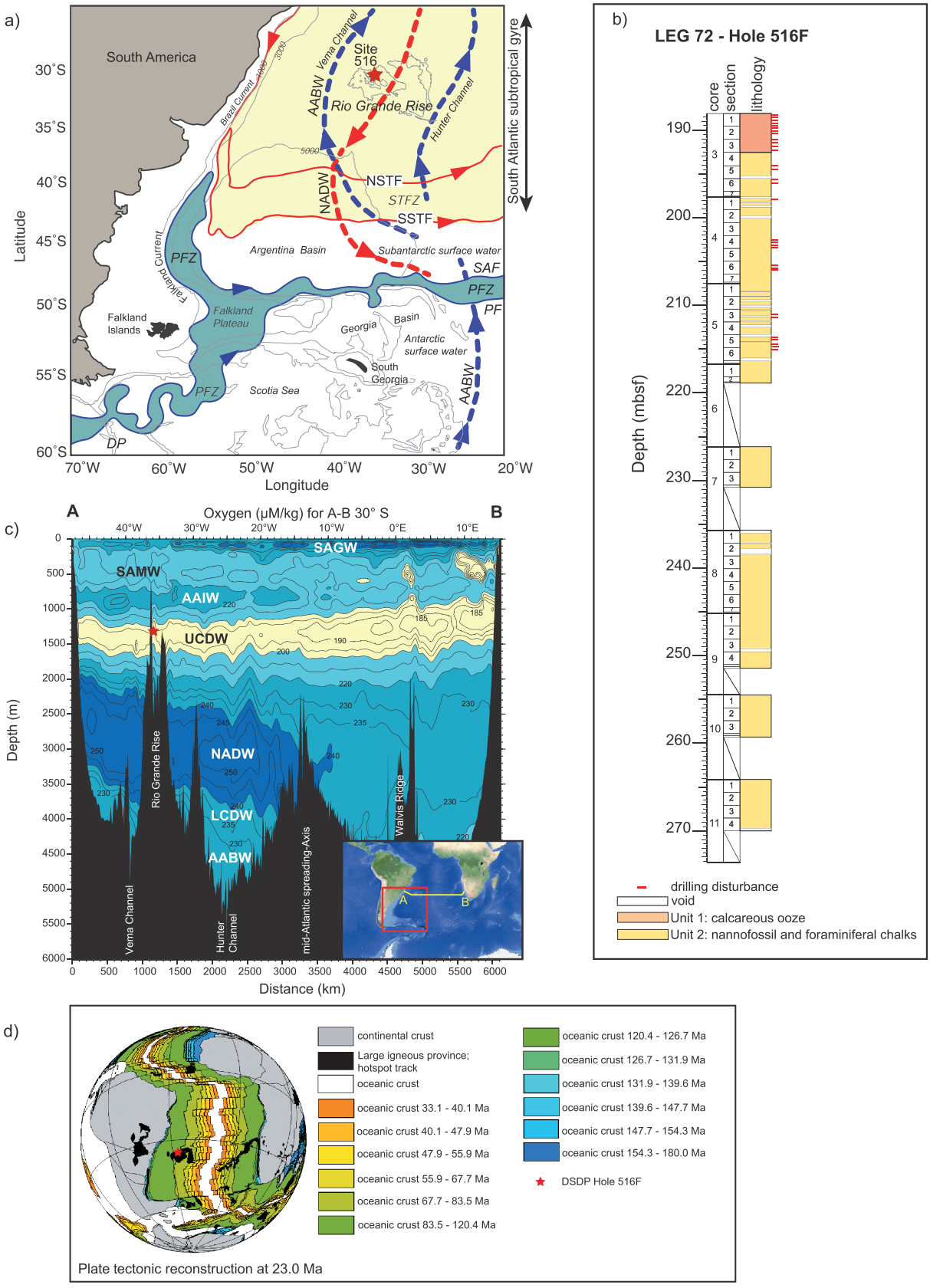
a)
South America
Site 516
Vema Channel
Hunter Channel
Rio Grande Rise
AABW
NADW
NSTF
STFZ
SSTF
South Atlantic subtropical gyre
Brazil Current
Falkland Current
PFZ
Argentina Basin
Subantarctic surface water
SAF
PF
Falkland Plateau
Falkland Islands
Georgia Basin
Antarctic surface water
South Georgia
Scotia Sea
DP
30°S
35°S
40°S
45°S
50°S
55°S
60°S
70°W
60°W
50°W
40°W
30°W
20°W
Latitude
Longitude
b)
LEG 72 - Hole 516F
core
section
lithology
Depth (mbsf)
drilling disturbance
void
Unit 1: calcareous ooze
Unit 2: nannofossil and foraminiferal chalks
c)
Oxygen (μM/kg) for A-B 30° S
A
B
SAGW
SAMW
AAIW
UCDW
NADW
LCDW
AABW
Rio Grande Rise
Walvis Ridge
Vema Channel
Hunter Channel
mid-Atlantic spreading-Axis
Depth (m)
Distance (km)
d)
continental crust
Large igneous province; hotspot track
oceanic crust
oceanic crust 33.1 - 40.1 Ma
oceanic crust 40.1 - 47.9 Ma
oceanic crust 47.9 - 55.9 Ma
oceanic crust 55.9 - 67.7 Ma
oceanic crust 67.7 - 83.5 Ma
oceanic crust 83.5 - 120.4 Ma
oceanic crust 120.4 - 126.7 Ma
oceanic crust 126.7 - 131.9 Ma
oceanic crust 131.9 - 139.6 Ma
oceanic crust 139.6 - 147.7 Ma
oceanic crust 147.7 - 154.3 Ma
oceanic crust 154.3 - 180.0 Ma
DSDP Hole 516F
Plate tectonic reconstruction at 23.0 Ma

3. Oceanographic Setting

DSDP Site 516 is today situated in the South Atlantic Subtropical Gyre, a largely wind-driven anticyclonic circulation that locally intensifies at its western boundary along the Brazil continental margin to form the southward flowing Brazil Current (Figure 1). At around 30°S, this meandering current has a volume transport of approximately 17.5×10^6 m^3/s [*Stramma*, 1989] that runs along the continental slope but also extends to the shelf. At around 40°S, the Brazil Current merges with the eastward trending Subtropical Frontal Zone (STFZ), which is a largely wind-forced feature, presumably with interleaved subtropical and subantarctic surface waters as evinced by northern and southern frontal components [cf. *Hamilton*, 2006]. South of the STFZ, subantarctic surface waters prevail except where the northern limit of the Antarctic Circumpolar Current (ACC), as marked by the Subantarctic Front (SAF), almost abuts the STFZ. This northward intrusion of the SAF results from topographic steering by the Falkland Plateau, which forces the SAF ~8° north together with the Polar Front (PF) before the PF continues its eastward passage, leaving the SAF to recirculate a further 10° to the north. This circulation pattern is driven by winds, eddies, and thermohaline processes and affects subsurface waters down to depths of about 1500 m [*Schmid et al.*, 2000]. The relative importance of these water masses is illustrated in Figure 1.

At greater depths, interactions between southward flowing North Atlantic Deep Water (NADW) and northward flowing Antarctic Bottom Water (AABW), which are among the densest ocean waters on Earth [*Orsi et al.*, 1999], determine the main path of deep water flow (Figure 1). Flows of AABW from the Weddell sector of Antarctica, together with Circumpolar Deep Water (CDW) tapped from the ACC, pass north as a deep western boundary current that typically occupies water depths that exceed 3500–4000 m [*Schmitz*, 1995]. AABW also passes into the Argentine Basin, propagating northward into the Brazil Basin after bifurcating into two strands through the Vema Channel and the Hunter Channel [*Murray and Reason*, 1999].

4. Previous Paleomagnetic Investigations

During Leg 72, 370 oriented samples were selected at low resolution (1 sample/3 m) from representative lithologies in Hole 516F, with a higher sampling density in the Paleogene and late Mesozoic intervals (i.e., below approximately 400 m bsf). Shipboard remanence measurements using a DIGICO spinner magnetometer were hampered by the low magnetization intensities of the biogenic sediments. Only a few samples were demagnetized on board using a peak alternating field (AF) demagnetization of 20 mT; remaining samples were analyzed post-cruise, using a peak AF of 20 mT or thermal demagnetization up to 280°C. Full details of the paleomagnetic protocols (e.g., number and spacing of demagnetization steps) are not available. About two-thirds of samples have normal polarity natural remanent magnetization (NRM) inclinations (i.e., negative or upward). NRM intensities were reduced by about 50% after AF demagnetization at 20 mT, which confirms the effectiveness of this technique in removing the normal polarity overprint [*Barker et al.*, 1983]. A polarity zonation was presented by *Berggren et al.* [1983] (Figure 2). Contrary to the report of *Barker et al.* [1983], the DSDP data bank does not contain remanence directions for the studied samples; it was, therefore, impossible to reinterpret these original data and integrate them with our new data. In addition to the magnetostratigraphic investigation, a preliminary

Figure 1. (a) Map with location of DSDP Site 516, Rio Grande Rise, with schematic representation of present-day upper ocean water masses and fronts and patterns of deepwater circulation [after *Reid et al.*, 1977; *Johnson*, 1983; *Larqué et al.*, 1997; *Murray and Reason*, 1999; *Stramma and England*, 1999; *Henderiks and Pagani*, 2007]. (b) Lithostratigraphic summary logs for DSDP Hole 516F [after *Barker et al.*, 1981, 1983]; m bsf—meters below sea floor. (c) Vertical section, along profile A-B, of dissolved oxygen content (μM/kg) plotted as a function of depth, with vertical exaggeration (depth: distance) of 1:1000 (modified from the WOCE Atlantic Ocean Atlas) [*Koltermann et al.*, 2011]. Inset: location of Figure 1a and the position of profile A-B. Abbreviations are DP, Drake Passage; PFZ, Polar Frontal Zone; PF, Polar Front; SAF, Subantarctic Front; STFZ, Subtropical Frontal Zone; SSTF, Southern Subtropical Front; NSTF, Northern Subtropical Front; SAGW, South Atlantic Gyre Water; SAMW, Southern Annular Mode Water (approximately 500 m deep); AAIW, Antarctic Intermediate Water (approximately 700–1100 m deep); UCDW, Upper Circumpolar Deep Water (approximately 1100–1600 m deep); NADW, North Atlantic Deep Water (1600–3600 m deep); LCDW, Lower Circumpolar Deep Water (approximately 3600–4500 m deep); and AABW, Antarctic Bottom Water (>4500 m deep). The position of Site 516 is indicated by a red star. (d) Plate tectonic reconstruction, centered on the south Atlantic, at the Oligocene-Miocene boundary [*Schettino and Scotese*, 2001].

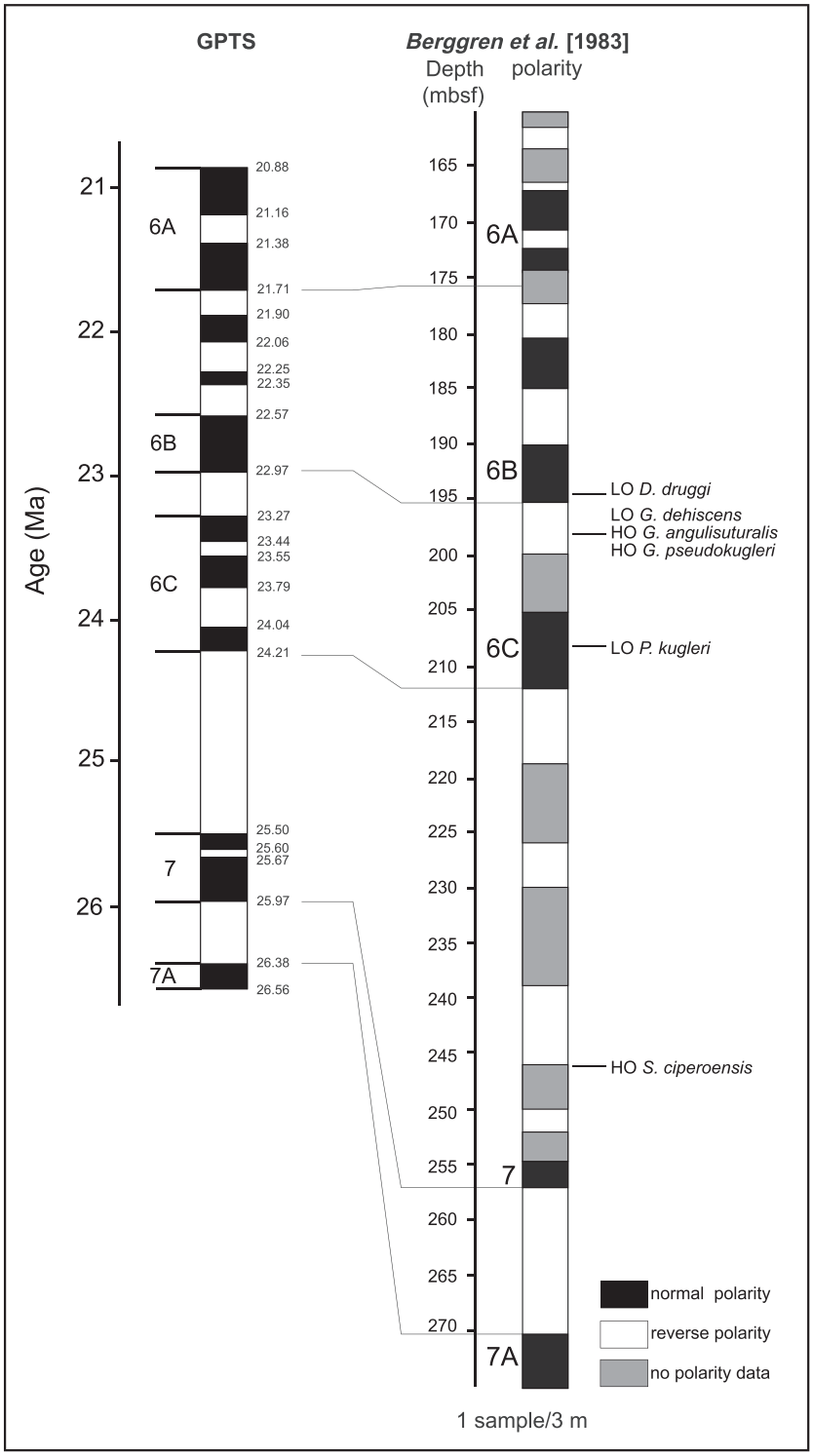

Figure 2. Correlation of the Hole 516F polarity zonation from *Berggren et al.* [1983] with the GPTS of *Berggren et al.* [1985].

rock magnetic investigation of sediments from Hole 516F was carried out by *Petrova et al.* [1983]. They focused only on the interval below core 19 (below approximately 340 m bsf), and inferred that magnetite, with lesser contributions from hematite, are the main magnetic minerals throughout most of Hole 516F. Iron hydroxides were detected in the Cretaceous portion of the core.

5. Sampling, Laboratory Procedures, and Analysis

For the present study, DSDP Hole 516F was sampled using standard ~8 cm^3 plastic cubes at the Integrated Ocean Drilling Program (IODP) Bremen Core Repository, where the core is now curated. One hundred thirty-nine samples were taken from the working halves of cores 516F-3R-2 to -11R-2, between depths of 189.72 and 266.7 m bsf. Core descriptions were used to select sampling locations. To collect samples, we used an extruder, which was pressed into the split core face keeping one of the flat sides of the extruder perpendicular to the up-hole direction. The extruder was then extracted full of sediment. A plunger on the end of the extruder allows the sediment to be extruded into a plastic sample box (2 cm × 2 cm × 2 cm), which has an arrow embedded in it. The sample was extruded such that the arrow points up-hole. The samples were oriented only with respect to vertical; the geocentric axial dipole field at the latitude of the coring site has an inclination of ±49.4°, which makes it feasible to reconstruct paleomagnetic polarity using only inclinations. With reference to available age models [*Berggren et al.*, 1983; *Pujol*, 1983; *Pagani et al.*, 2000], our sampling was designed to span the upper Oligocene to lowest Miocene section. At the same time, 219 samples were also collected from the working halves of cores 516F-3R-1 to -11R-2 (between depths of 188.18 and 266.94 m bsf) for calcareous nannofossil and planktonic foraminiferal biostratigraphic analysis with an average resolution of approximately 25 cm [*Gennari et al.*, 2014]. This sample spacing greatly enhances the resolution and robustness of the biostratigraphy within the interval of interest compared to previous studies.

To minimize sample dehydration and alteration, samples were packed in sealed bags and were stored in a refrigerated room until they were processed at the Istituto Nazionale di Geofisica e Vulcanologia, Rome. Natural and artificial magnetizations were measured at room temperature using a narrow-access pass through 2-G Enterprises cryogenic magnetometer housed in a Lodestar Magnetics shielded room. After measurement of the NRM, samples were AF-demagnetized at successive peak fields of 5, 10, 15, 20, 25, 30, 35, 40, 45, 50, 60, 70, 80, and 100 mT. NRM stability was assessed using vector component diagrams [*Zijderveld*, 1967]. Principal component analysis [*Kirschvink*, 1980] was used to calculate characteristic remanent magnetization (ChRM) directions, with linear best fits calculated from a minimum of three demagnetization steps using the PuffinPlot paleomagnetic analysis application [*Lurcock and Wilson*, 2012].

Following AF demagnetization of the NRM, rock magnetic analyses were conducted on the same samples to estimate downcore variations in the composition, concentration, and grain size of magnetic minerals. All data were normalized by mass because sample volumes are irregular. Low-field magnetic susceptibility (κ) was measured using an AGICO KLY-2 Kappabridge magnetic susceptibility meter with a field of 0.1 mT at a frequency of 470 Hz. An anhysteretic remanent magnetization (ARM) was imparted by using a 0.05 mT direct current (DC) bias field superimposed on a 100 mT peak AF and by translating u-channels through the AF and DC coil system at 10 cm/s, which is the lowest speed allowed by the control software. The resulting ARM was then measured. An isothermal remanent magnetization (IRM) was imparted with a DC field of 900 mT (IRM_{900mT}) and demagnetized in a 100 mT backfield ($-IRM_{100mT}$) using a 2-G Enterprises solenoid aligned with the magnetometer. From these measurements, in order to characterize the coercivity of the magnetic minerals, we calculated the *S* ratio $S_{100mT} = (1 - IRM_{-100mT}/IRM_{900mT})/2$ [*Bloemendal* et al., 1992].

Using selected powder samples, a high-coercivity percentage S ratio (S_H) was calculated as $100 \times (-IRM_{-300mT}/IRM_{2700mT})$ to determine the contribution of the hard component to the overall magnetization. The IRM at 2.7 T was imparted with a 2-G Enterprises pulse magnetizer, using a custom-made plexiglas sample holder suitable for containing the 15 mL powder-filled gel caps used for measurements with a Princeton Measurements Corporation Model 3900 Micromag vibrating sample magnetometer (VSM). The magnetization of the empty plexiglas holder was measured after IRM acquisition at 2.7 T and at 0.1 T and was subtracted from measured sample IRM values.

IRM acquisition and backfield demagnetization, hysteresis loops, and first-order reversal curve (FORC) measurements [*Pike et al.*, 1999; *Roberts et al.*, 2000, 2014] were made using the VSM. Samples were taken from representative intervals with sufficiently strong magnetizations to investigate coercivity and magnetostatic interaction distributions for the magnetic particles. For weakly magnetized samples, we

made multiple measurement runs to stack results and increase the signal-to-noise ratio of the FORC distribution [*Heslop and Roberts*, 2012]. FORC diagrams were processed using the FORCinel software [*Harrison and Feinberg*, 2008]. Continuously monitored temperature dependence of the low-field magnetic susceptibility (κ) (up to 700°C) was measured in air using an AGICO CS-3 furnace-equipped Kappabridge KLY-3 system (field = 200 A/m; frequency = 976 Hz), in order to determine the characteristic Curie or Néel temperatures of magnetic minerals [*Hrouda*, 1994].

Sediment particle size distributions were determined for the same samples used for magnetic analyses. Samples were dissolved in distilled water and the particle size distribution was measured using a Mastersizer 2000 laser diffraction granulometer and associated Malvern Instruments Ltd. dispersion units at the Physics and Earth Science Department "Macedonio Melloni," University of Parma [e.g., *Storti and Balsamo*, 2010, and references therein]. Fine particles tend to aggregate during measurements; therefore, samples were subjected to ultrasound treatment for 8 min to disaggregate particle flocs and to remove encrustations on foraminiferal shells. Laboratory tests indicate that particle size distributions were reproducible after 8 min of ultrasound treatment.

The volume and density of the samples used for micropaleontological analyses [*Gennari et al.*, 2014] were also measured using a single-sample station Ultrapyc 1200e gas pycnometer, which can measure the true volume of even porous and granular solids. Before analysis, samples were dried in an oven for 1 day at 40°C. Each analysis was repeated 10 times; both the averages and the standard deviations of the repeated density measurements are reported. The dry bulk density of the sediments was multiplied by the linear sedimentation rate to calculate the mass accumulation rate (MAR). MAR is expressed as gram dry sediment accumulating per cm^{-2} per kyr ($g\,cm^{-2}\,kyr^{-1}$). The planktonic foraminiferal accumulation rate (PFAR) is considered a proxy for surface water productivity [e.g., *Mojtahid et al.,* 2013], since the growth rate and the overall standing stock of the living planktonic foraminiferal community depend on food availability (marine primary producers) [*Bé et al.,* 1981*; Watkins et al.*, 1998]. The PFAR was calculated by multiplying the MAR by the number of planktonic foraminifera per gram of dry sediment (number of tests $cm^{-2}\,kyr^{-1}$). Planktonic foraminifera in the sediment can be subjected to dissolution, which can substantially lower their number and affect the PFAR. We therefore calculated the fragmentation index (FI) [*Berger*, 1970], which is the most commonly used dissolution index [e.g., *Kucera*, 2007]. FI is defined as the number of fragmented planktonic foraminiferal shells (F) divided by the sum of F and complete shells (P), expressed as a percentage: $(F/(F+P)\times 100)$.

6. Results and Discussion

6.1. Magnetic Properties

Mass-normalized NRM intensities from Hole 516F range from 1.13×10^{-9} ($A\,m^2\,kg^{-1}$) to 1.57×10^{-6} ($A\,m^2\,kg^{-1}$) (Figure 3); κ values range from -6.7×10^{-9} ($m^3\,kg^{-1}$) to 5.97×10^{-8} ($m^3\,kg^{-1}$). Downcore κ variations are associated with similar changes in ARM and IRM, which suggests that these fluctuations are mainly controlled by changes in magnetic mineral concentration; notably, all of these records contain a few spikes, particularly in cores 3–5 (Figure 3). These relatively narrow spikes coincide with horizons with visible sparse, fine, dark gray clasts. *Bryan and Duncan* [1983] reported similar features in Eocene horizons from Hole 516F and concluded that the clasts were derived from a mixed volcanic/plutonic terrane, possibly with a direct contribution from contemporary volcanic ash falls. Our preliminary analyses of the clasts using a scanning electron microscope with energy dispersive spectrometry (SEM-EDS) indicate the presence of ilmenite, quartz, and amphibole (E. Salvioli Mariani, University of Parma, personal communication, 2014), which suggests that the clasts have a volcanic origin. There was no known contemporaneous volcanic or ice-rafting activity in the region, which suggests that they probably consist of redeposited material scoured during transient variations in bottom water flow patterns from nearby sites on the Rio Grande Rise.

Relatively low S ratios throughout the studied stratigraphic interval indicate the presence of high-coercivity magnetic minerals (e.g., hematite); low ARM and IRM inclinations also indicate that, for some samples, the peak fields used to impart the ARM and IRM were not fully able to realign the magnetic moments of remanence carriers (Figure 3). The S ratio is only a meaningful measure of relative ferrimagnetic mineral content for magnetic minerals with saturation fields less than 1 T. For two selected samples, from depths

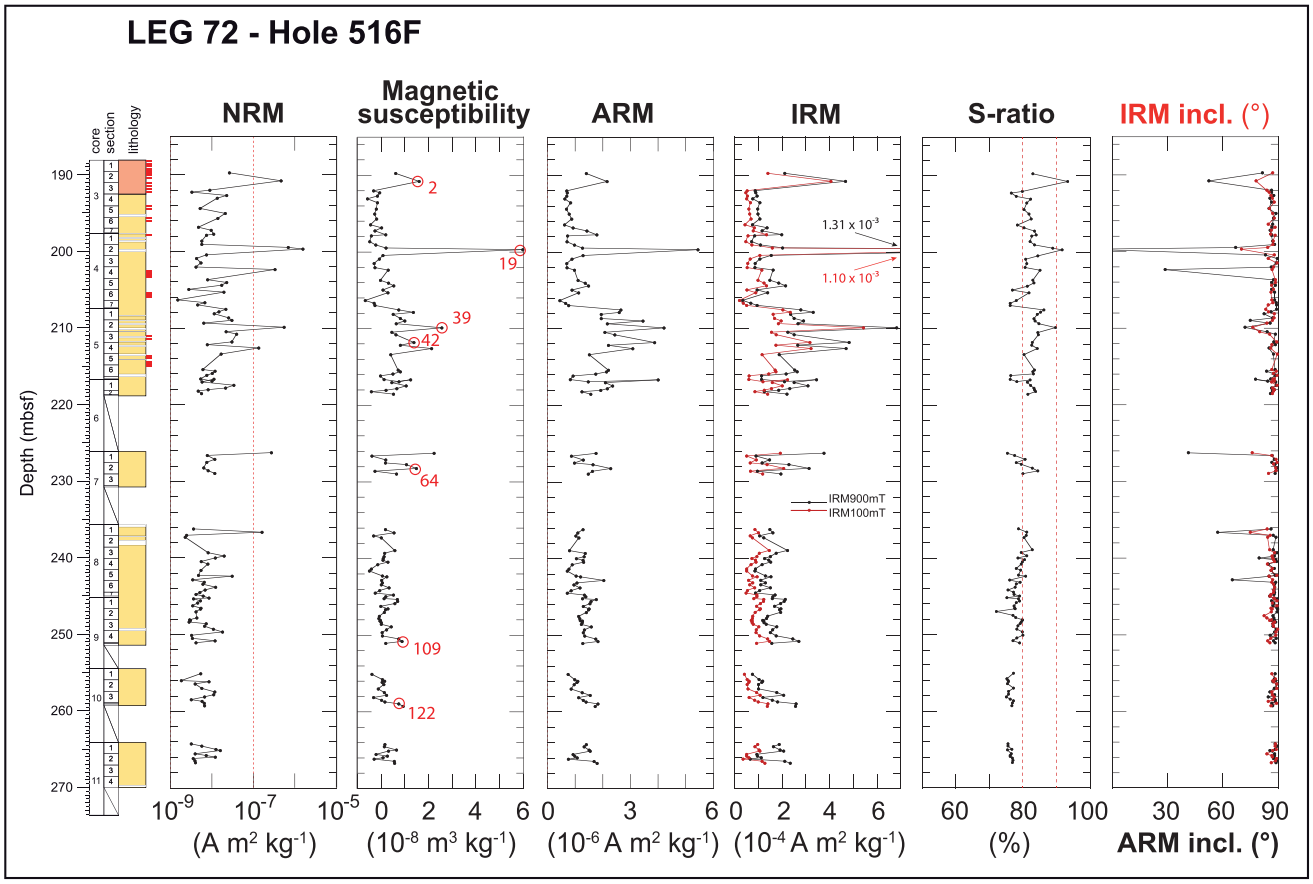

Figure 3. Mineral magnetic data for DSDP Hole 516F. Stratigraphic variations of intensity of NRM, κ, ARM, IRM_{100mT}, IRM_{900mT}, S-ratio% = 100 × (1 − IRM_{-100mT}/IRM_{900mT})/2, IRM_{900mT}, and ARM inclinations.

of 196.84 and 199.69 m bsf, S is 80.4% and 91.8%, respectively, while S_H decreases to 68.8% and 72.8%, respectively, which indicates that a large fraction of the IRM is carried by high-coercivity magnetic phases. Differences between S and S_H confirm that a DC field of 900 mT cannot be considered a saturating field for these samples. The presence of mixtures of high-coercivity hematite with low-coercivity magnetite is supported by the temperature dependence of κ (Figure 4). A κ-T curve for sample 516-19 from a magnetic spike at 199.69 m bsf has major inflections at approximately 580°C and 680°C (albeit noisy), which suggests a mixture of magnetite and hematite. The cooling curve has higher overall κ than the heating curve, which indicates production of new magnetic phases during heating.

FORC diagrams were produced to characterize magnetostatic interactions and magnetic domain state distributions in the studied samples. The FORC diagram for sample 516-19 (Figure 5a) has a peak near the origin and an additional secondary peak at about 15 mT, which is consistent with the presence of low-coercivity fine (single-domain, SD) and ultrafine (superparamagnetic, SP) magnetite fractions [*Pike et al.*, 2001]. The FORC diagram for sample 516-59 is dominated by a low-coercivity SP component, which is confirmed by viscous decay of magnetization in Figure 5c. The contribution of SP grains to the remanence was calculated using the method of *Wang et al.* [2010]. Assuming that the room-temperature viscous decay of the IRM 100 s after its application is due to thermal relaxation of the magnetization carried by the SP fraction, the SP particle percentage is estimated by $M_{RS}(SP)\% = 100(M_{RS0} - M_{RS100})/M_{RS0}$, where M_{RS0} is the remanence measured after application of a 1 T "saturating field" and M_{RS100} is measured 100 s after field application. For this sample, we estimate the SP content at 17%. The presence and relative increase of ultrafine SP particles in samples 516-19 and 516-59 is associated with the corresponding magnetic susceptibility peaks. Outside these spikes, meaningful FORC distributions could not be obtained even after stacking multiple runs following the method of *Heslop and Roberts* [2012].

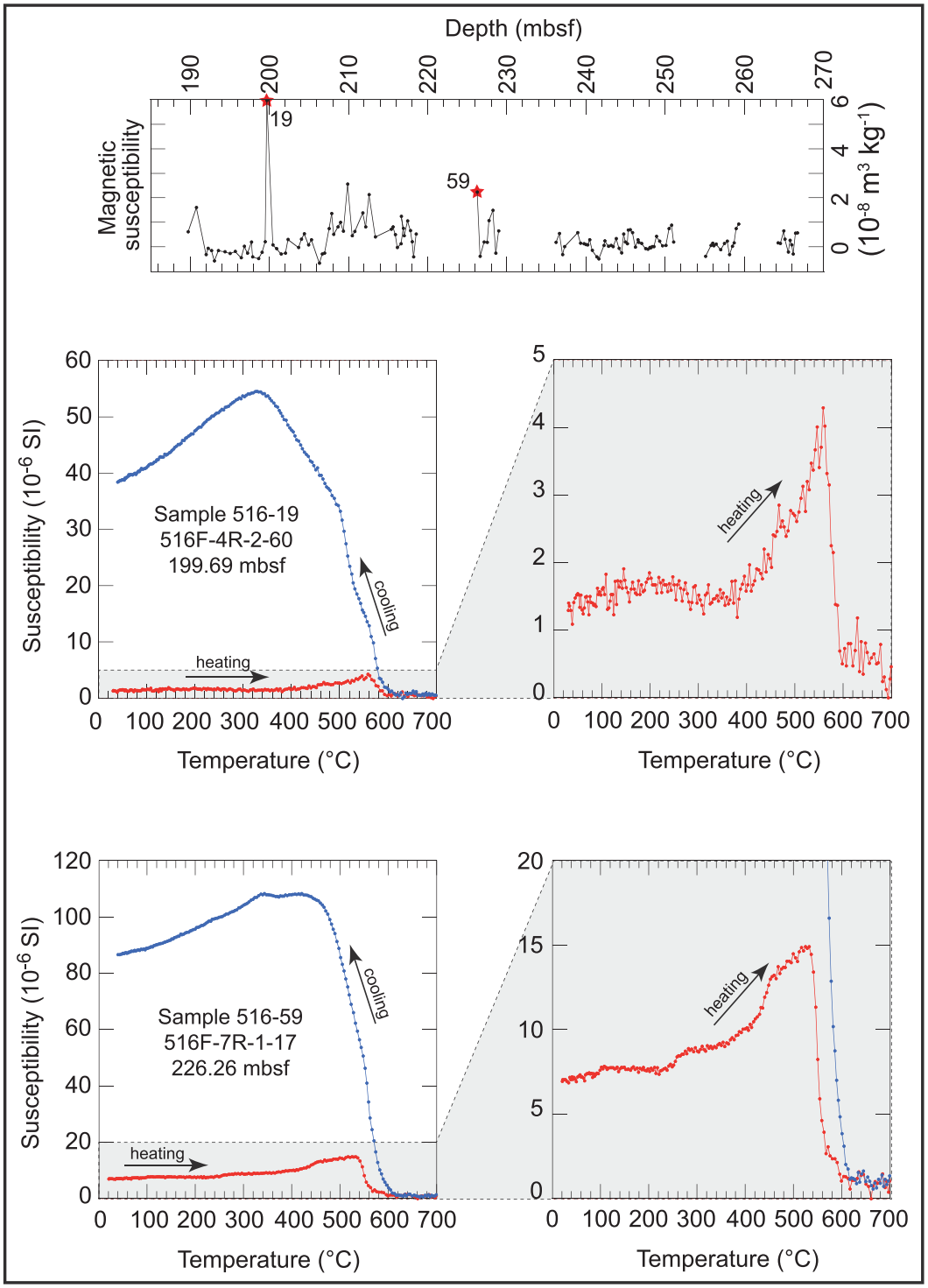

Figure 4. Temperature dependence of κ (up to 700°C) for two representative samples 516-19 (516F-4R-2-60) and 516-59 (516F-7R-1-17). For both samples the main Curie temperatures at 580°C suggest the presence of magnetite. κ-*T* data for sample 516-59 contain an additional inflection at 680°C, which suggests the concomitant presence of hematite. The cooling curves have a higher κ than the heating curves, which indicates the production of new magnetic phases during heating. The stratigraphic positions of these samples are indicated on the magnetic susceptibility log at the top of the figure.

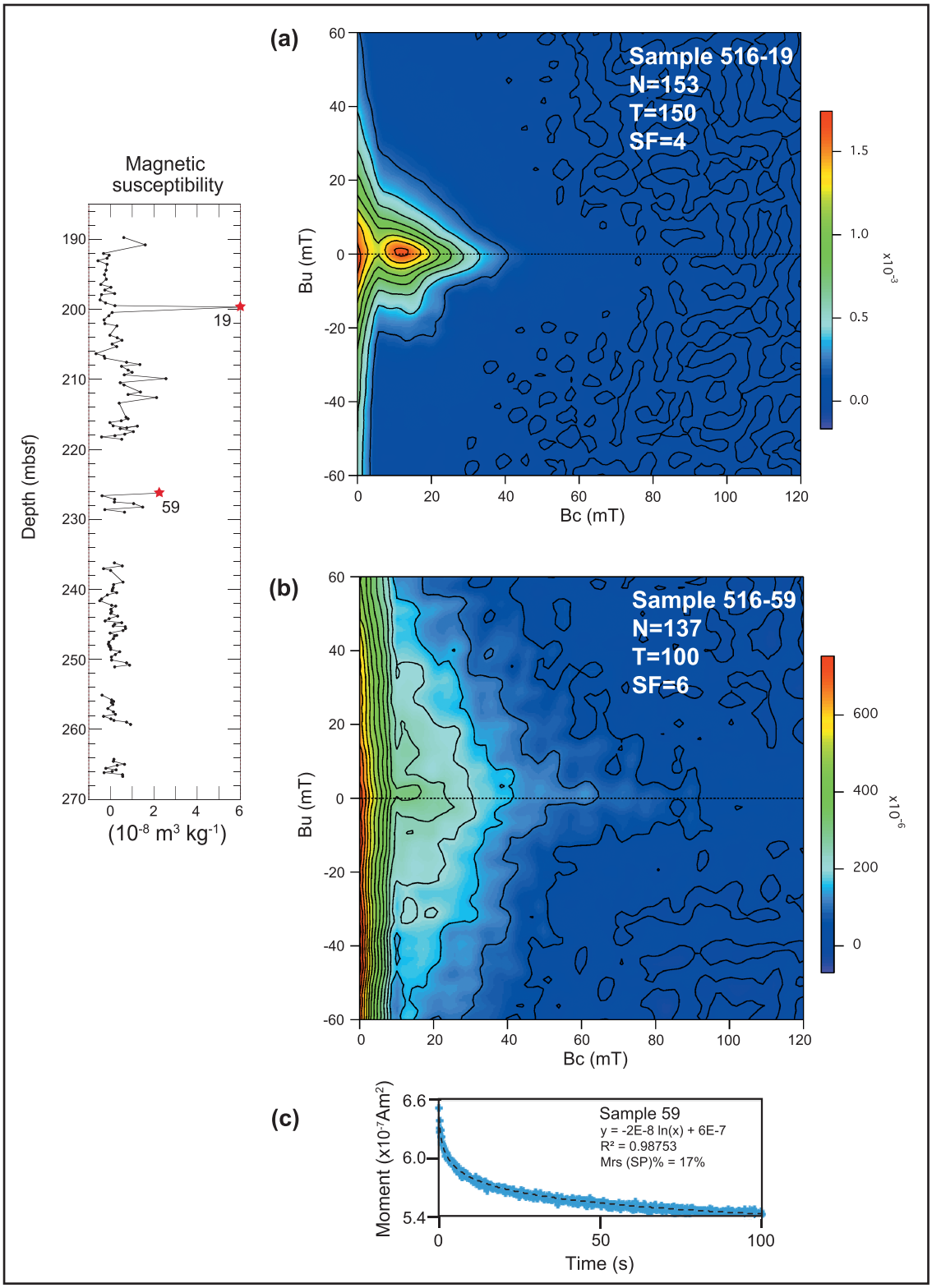

Figure 5. (a, b) FORC diagrams for two representative samples (516-19 at 199.69 m bsf, 516-59 at 226.26 m bsf) with coercivity and magnetostatic interaction distributions. SF = smoothing factor [see *Roberts et al.*, 2000, 2014]. (c) Decay of a 1 T M_{rs} imparted to sample 516-59 over 100 s; M_{rs}(SP)% and parameters for the logarithmic fit are reported [*Wang et al.*, 2010]. For the FORC diagrams, N = number of measured FORCs and T = averaging time in milliseconds.

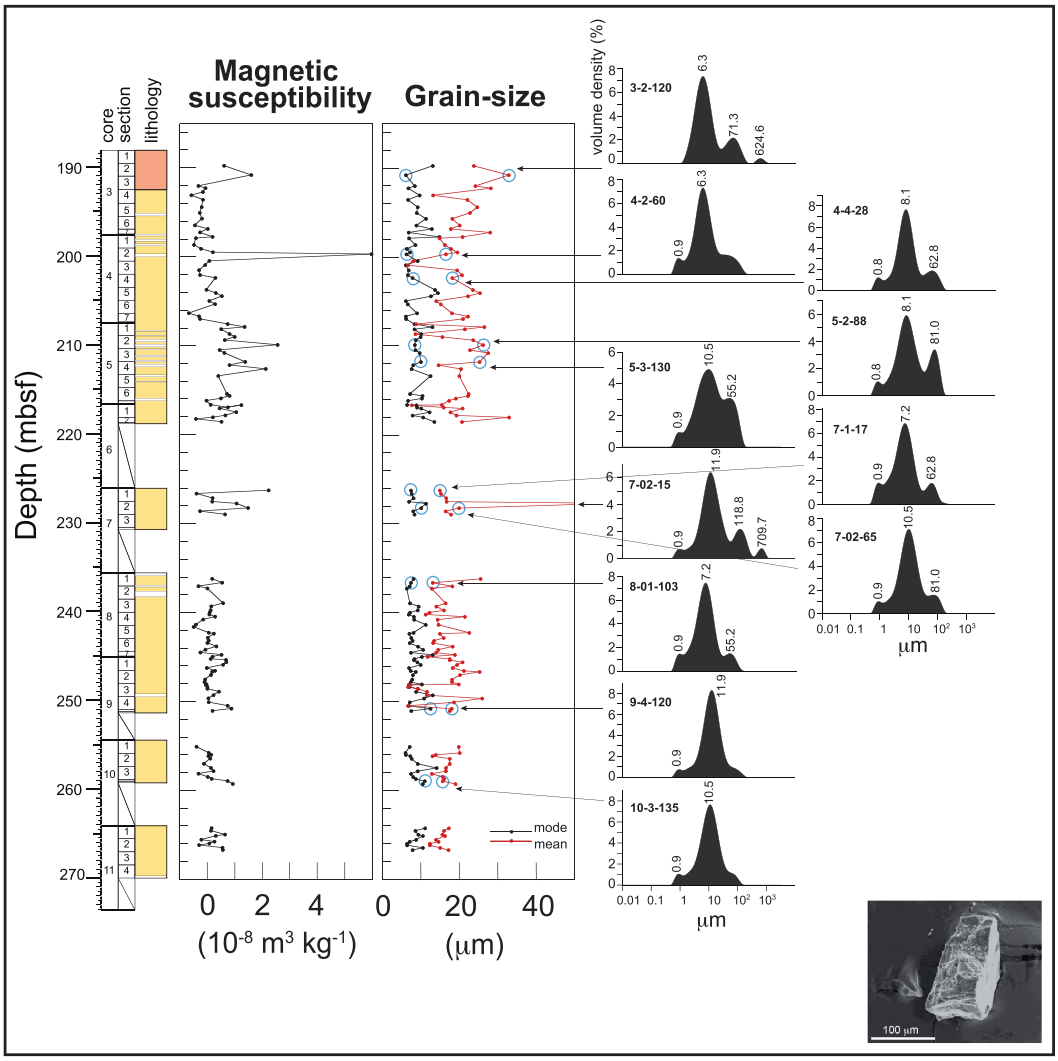

Figure 6. Lithology, κ, and grain size distribution by laser granulometry for DSDP Hole 516F, plotted as a function of depth. Granulometric curves for eleven representative samples are shown on the right. Inset: SEM image of a volcanic clast identified in sample 516-19 at 199.69 m bsf.

6.2. Particle Size Analysis

Sediment particle size distributions can provide information on the geological processes recorded at DSDP Site 516 (see discussion in section 6.5, "The new age model and implications for paleoclimate and paleoceanographic changes"). Particle size distributions are trimodal for most of the studied samples. Variation in the particle size distributions is not strongly correlated with magnetic property variations (Figure 6). The abiotic sediment fraction is represented by the fine (clay) mode centered at around 0.9 μm and by another mode above 600 μm. The latter is attributable to sporadic volcanic clasts, as revealed by SEM observations (inset in Figure 6). The main particle size mode is between 6.3 and 10.5 μm; microscopic observations indicate that it is due to coccoliths. Within the coarse mode, particle size varies between 55 and 118 μm due to foraminiferal assemblages. From about 230 m bsf upward, increased between-sample variability indicates a more heterogeneous sediment composition.

6.3. Paleomagnetic Behavior and Polarity Zonation

As described above, NRM intensities are generally low throughout the core with values ranging between 1.13×10^{-9} A m^2 kg^{-1} and 1.57×10^{-6} A m^2 kg^{-1}, with a few thin higher intensity intervals (Figure 3).

Although demagnetization paths are often noisy, probably because of weak NRM intensities, stepwise AF demagnetization enabled isolation of the ChRM component for 78% of samples analyzed, which allows construction of a magnetic polarity zonation.

ChRM directions for most analyzed samples tend toward the origin of the vector component plots, with maximum angular deviation (MAD) values generally $< 8°$ (Figures 7 and 8). A few samples are characterized by shallow paleomagnetic inclinations (Figure 7; sample 516-81 at 242.35 m bsf) and, at some depths, higher-coercivity components are present (Figure 7; samples 516-19 at 199.69 m bsf, 516-39 at 209.87 m bsf, 516-68 at 236.62 m bsf). These spurious paleomagnetic results coincide with the above-mentioned sharp NRM, ARM, and IRM peaks (Figure 3).

The ChRM inclinations enable delineation of eight magnetozones, which are defined using at least two consecutive samples with inclinations distinctly different from neighboring intervals (Figure 8). In some magnetozones, occasional isolated samples have polarities opposite to those of the rest of the magnetozone. Such isolated samples are not used to define polarity zones. Magnetozones are labeled according to their polarity (i.e., *N* = normal or *R* = reversed), with progressive downcore numbering within the hole (i.e., 1, 2, and 3).

6.4. Age Model

We used the GPTS of *Gradstein et al.* [2012] to develop an age model for the studied interval. We used new quantitative analyses of calcareous nannofossil and planktonic foraminiferal assemblages [*Gennari et al.*, 2014] to refine the age model of *Berggren et al.* [1983]. Our magnetostratigraphic interpretation for Hole 516F is presented in Figure 9 along with biostratigraphic data and the stratigraphic uncertainties associated with each datum (Tables 1 and 2). In the upper part of the studied succession, the lowest occurrence (LO) of *Sphenolithus cometa* (reported as falling in subchron C6Bn.2n at DSDP Site 563) [*Maiorano and Monechi*, 1998], the lowest common occurrence (LCO) of *Paragloborotalia kugleri* (which is time equivalent to the LO of *P. kugleri* at Atlantic low-latitudes and calibrated at 22.96 Ma by *Lourens et al.* [2004]), and the highest occurrence (HO) of *Sphenolithus capricornutus* (calibrated at 22.97 Ma in the North Pacific Ocean) [*Gradstein et al.*, 2012] suggest a correlation from subchrons C6Bn.2n (21.992 Ma) to C6Cn.2n (23.030 Ma). The Oligocene-Miocene boundary occurs at approximately 216 m bsf, i.e., at the base of subchron C6Cn.2n (Table 2). Below this interval, the HO and LO of *Sphenolithus delphix* (calibrated at ODP Site 1218 at 23.06 and 23.38 Ma, respectively) [*Backman et al.*, 2012], the HO of *Sphenolithus ciperoensis* (associated with Chron C7n) [e.g., *Blaj et al.*, 2009] near the bottom of the record, suggest a correlation from subchrons C6Cn.2r (23.030 Ma) to C7r (24.761 Ma). The short ($<$70 kyr) subchrons C6Cn.3n and C7n.1n could not be identified unambiguously in the studied interval because of intervals with low core recovery.

6.5. The New Age Model and Implications for Paleoclimate and Paleoceanographic Changes

With the improved age model, the average sedimentation rate increases progressively, doubling at 23.9 Ma and then doubling again to 6.5 cm/kyr at the Mi-1 event at the Oligocene-Miocene boundary (22.9 Ma, base of C6n.2n) [*Miller et al.*, 1991; *Pälike et al.*, 2006] (Figures 9–11). Increased sedimentation was apparently not related to increased terrigenous input, since the carbonate component remained at 77–80%, with a biogenic silica content of ~10% and a relatively invariant fine clay component (a potential indicator of windblown dust) (Figure 6). The increase appears, rather, to have resulted from higher biogenic production, as indicated by the number of planktonic foraminiferal tests per gram of sediment and by the PFAR index (Figure 12), which is a proxy for surface water productivity [e.g., *Mojtahid et al.*, 2013, and references therein]. The PFAR index is generally low during the late Oligocene, while indicating two intervals of increased productivity, from 215 to 207 m bsf and from 197 to 190 m bsf. High PFAR values are associated with elevated sedimentation rates, fragmentation index, and κ in the time interval corresponding to Mi-1 (Figure 12). However, high values of FI, which indicate increasing dissolution, do not bias the increased productivity during Mi-1, as inferred from concomitant higher PFAR values.

Increased paleoproductivity during the Mi-1 event is also observed at Southern Ocean ODP Site 1090 and at southeast Atlantic ODP Site 1265 (Figure 13) [*Diester-Haass et al.*, 2011]. At sites 1265 and 1090 increased paleoproductivity started in the late Oligocene, at 23.5 Ma and 24 Ma, respectively, with maxima centered at the Oligocene-Miocene boundary. At Site 516, no-recovery intervals below the Oligocene-Miocene

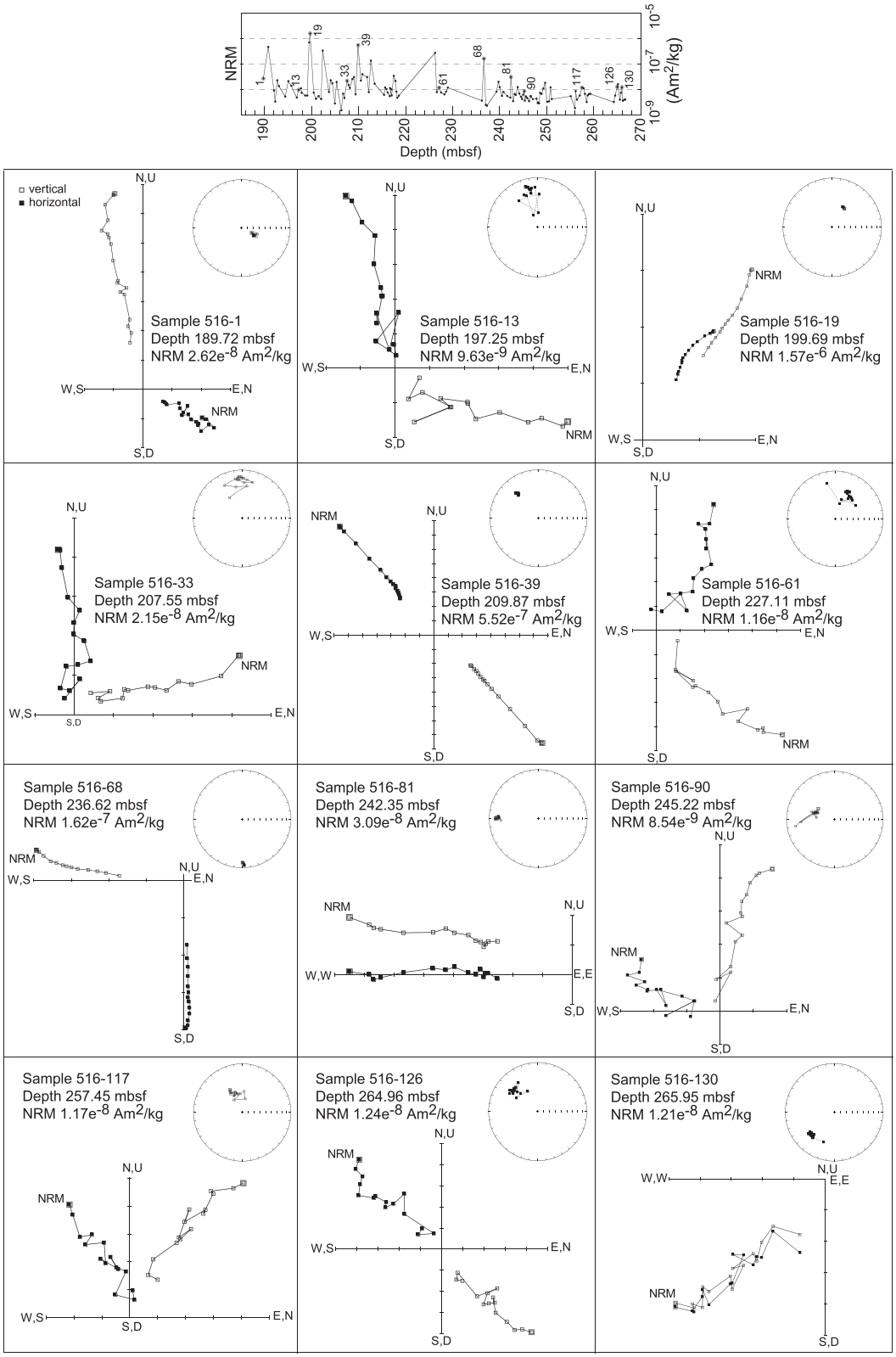

Figure 7. AF (alternating field) demagnetization behavior for 12 representative samples from Hole 516F. For the vector component diagrams, open (closed) symbols represent projections onto the vertical (horizontal) plane. The stereoplots are equal-area projections, with solid (open) symbols representing points projected onto the lower (upper) hemisphere. The cores were not azimuthally oriented; declinations are reported in the laboratory coordinate system with respect to the split face of the core. Plots were produced using PuffinPlot [*Lurcock and Wilson*, 2012]. A downcore log of NRM intensity is shown at the top of the figure with the positions of samples indicated.

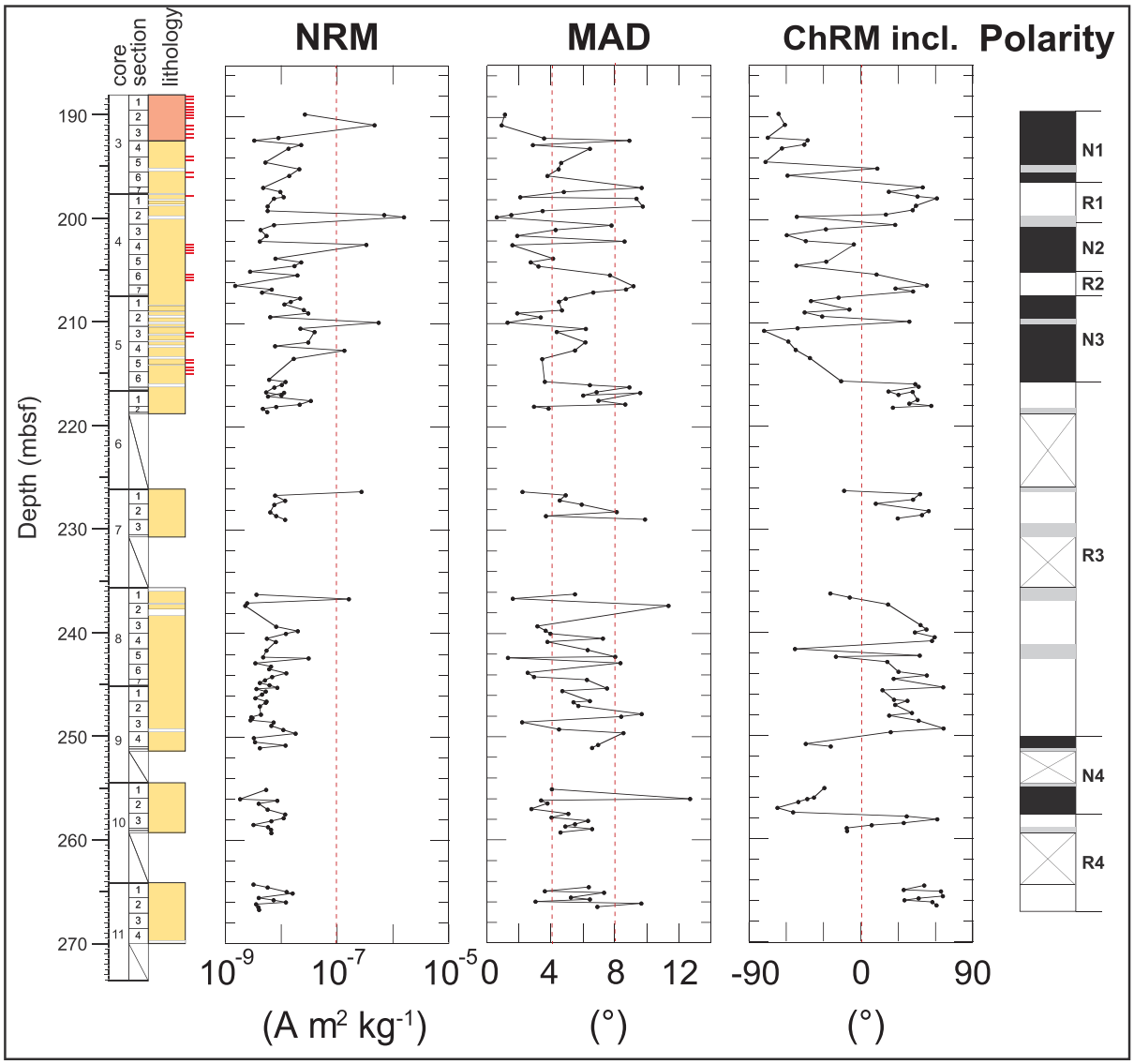

Figure 8. Lithology (symbols as in Figure 1), downcore variations of NRM intensity, MAD, ChRM inclination, and magnetic polarity zonation (black = normal polarity and white = reverse polarity).

boundary hinder straightforward identification of a comparable pattern. However, a first peak at 23.4 Ma is present and is comparable with the coeval peak at Site 1265. Paleoproductivity maxima at the Oligocene-Miocene boundary are clearly evident at all of these sites. Compared with modeled $\delta^{18}O$ records associated with Antarctic ice sheet expansion [*Liebrand et al.*, 2011], we observe that at sites 1090 and 516, paleoproductivity maxima coincided with the deglaciation phase at the end of Mi-1, which is characterized by 100 kyr glacial cycles of lower amplitude than the $\delta^{18}O$ decrease during Mi-1.

The later PFAR maximum (197–190 m bsf) is associated with high sandy fraction percentages (>63 μm) of the residue and may be associated with one of the minor glacial events that follows Mi-1 [*Billups et al.*, 2002; *Liebrand et al.*, 2011] (Figure 13). Correlation of this maximum with a specific glacial event is difficult: age control for the uppermost part of the core is uncertain because the last reliable age control point is at the base of C6Bn.2n (22.268 Ma, 196.26 m bsf).

Our data provide new evidence for an expansion of the areal extent of increased productivity and carbon burial in the southwest Atlantic Ocean basin around the time of Mi-1. The higher rates of paleoproductivity observed from around 23.4 Ma are likely to have caused increased organic carbon burial,

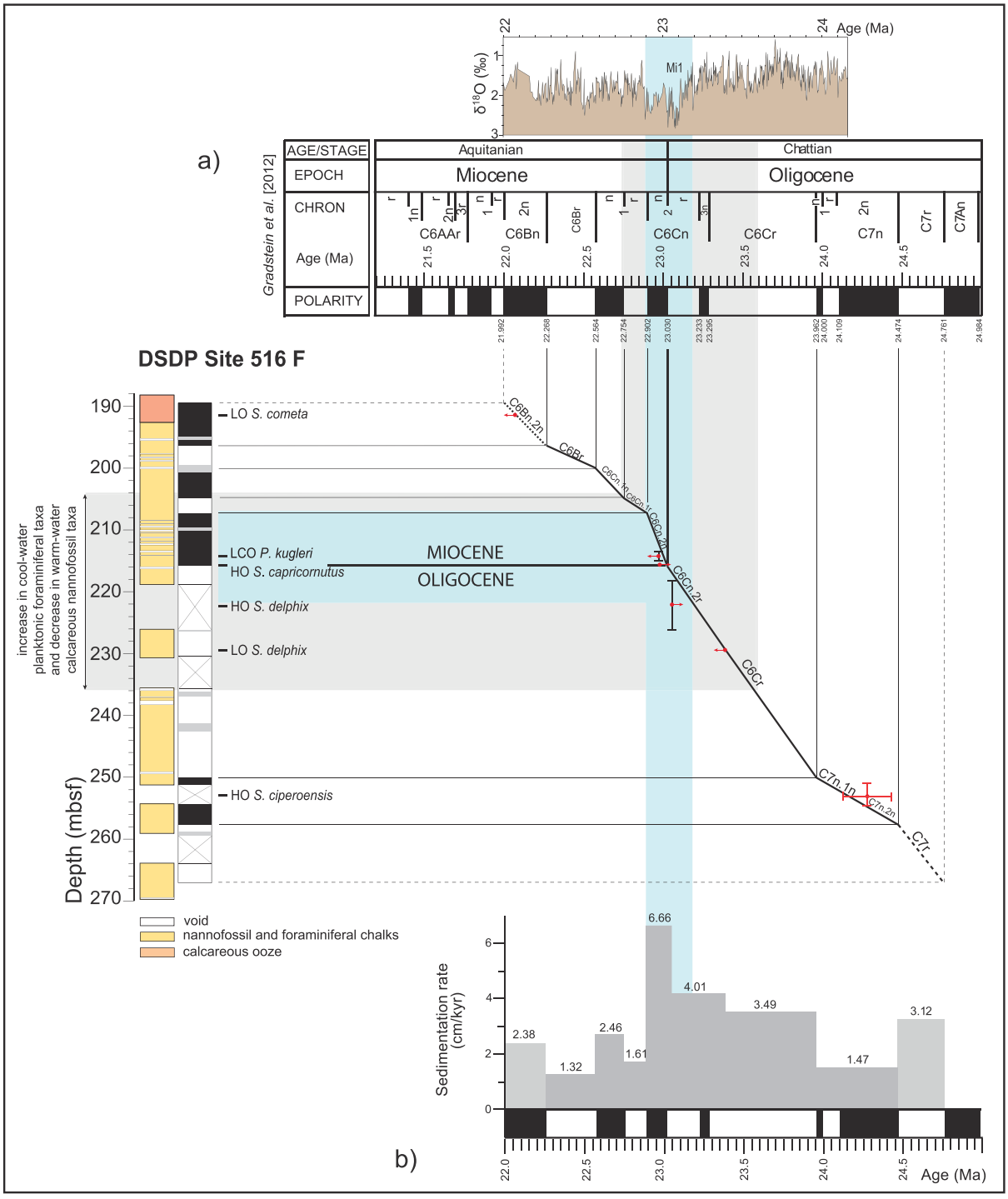

Figure 9. (a) Correlation of the new magnetic polarity zonation from Hole 516F with the GPTS of *Gradstein et al.* [2012]; and (b) sedimentation rate variations from the studied interval of DSDP Site 516F. Black (white) indicates normal (reversed) polarity. Calcareous nannofossil and planktonic foraminiferal datums used to constrain the age model are described by *Gennari et al.* [2014]. At the top, the ODP Site 1090 benthic δ^{18}O record is shown [*Billups et al.*, 2002, 2004]. With Analyseries [*Paillard et al.*, 1996], we used the Site 1090 benthic foraminiferal δ^{18}O record as a "Series" file and the polarity chron boundaries (from C6Bn through C7r) from *Channell et al.* [2003], with ages from *Gradstein et al.* [2012] as "Pointers" to stepwise interpolate between tie-points to create the time scale. The cyan vertical shaded area corresponds to the interval that records the Mi-1 event [*Miller et al.*, 1991, Table 4 therein]. The gray shaded area corresponds to the interval with increased cool-water planktonic foraminiferal taxa and decreased warm-water calcareous nannofossil taxa.

Table 1. Biostratigraphic Events in Hole 516F [*Gennari et al.*, 2014][a]

Bioevent	*Lourens et al.* [2004]	*Maiorano and Monechi* [1998]	*Gradstein et al.* [2012] **Shackleton et al.* [2000]	*Backman et al.* [2012]	Depth Minimum (m bsf)	Depth Maximum (m bsf)	Mean Depth (m bsf)
LO *S. cometa*		in C6Bn.2n			191.34	191.71	191.53
LCO *P. kugleri*	22.96				213.88	214.68	214.28
HO *S. capricornutus*			22.97		215.78	215.8	215.79
HO *S. delphix*				23.06	218.59	226.35	222.47
LO *S. delphix*				23.38	229.65	229.95	229.80
HO *S. ciperoensis*			24.13*–24.43		251.16	254.77	252.97

[a]HO = Highest Occurrence, LO = Lowest Occurrence, and LCO = Lowest Common Occurrence.
*The asterisk in Table 1 denotes the reference of 24.13 Ma dating.

which, in turn, would have caused a CO_2 drawdown. The increase in areal extent of carbon burial suggests that a tipping point in carbon burial and the resulting CO_2 drawdown may have been reached, thereby initiating the climatic cooling and ice volume increase at Mi-1. It is difficult to draw precise conclusions about the relationship between the Mi-1 $\delta^{18}O$ maximum and our productivity record, since we lack data for the central 23.3–23.1 Ma period, but the PFAR minimum at 23.05 Ma, shortly before the end of Mi-1 and preceding a 150 kyr peak in PFAR suggests that, at Site 516, the relationship between productivity and glaciation was more complex than the positive feedback inferred by *Diester-Haass et al.* [2011] for Site 1090.

Higher-sedimentation rates also occurred at ~24.5 Ma, which correlates with the Oi2D $\delta^{18}O$ glacial event [*Boulila et al.,* 2011] (Figures 10 and 11). Our records do not extend to the period that precedes the Oi2D event, so it is possible that this increase may have been part of a longer-term trend, rather than a single peak associated with Oi2D. However, a modest increase in paleoproductivity is also documented at Site 1090, which supports the notion that a link also exists between carbon cycling and climate during the Oi2D event [*Diester-Haass et al.*, 2011] (Figure 13). In addition, the areal extent and amount of the productivity increase appears to have been related to the amount of ice volume expansion for each event, with a larger productivity increase at Mi-1 and subsequent events associated with considerably greater ice volume (~50% increase to 125% of the modern-day ice volume [*Pekar et al.*, 2006; *Liebrand et al.,* 2011; *Mawbey and Lear*, 2013]) compared to a more modest increase in productivity increase during Oi2D and a smaller ice volume change (~35% increase to near modern-day size) [*Pekar et al.*, 2006]. This relationship between productivity and climate is also observed immediately after Mi-1, with an abrupt productivity decrease around 100 kyr after the end of the $\delta^{18}O$ maximum, which suggests that deglaciation was connected to decreased carbon burial in the ocean, as supported by dissolution events observed at deep water sites [*Mawbey and Lear*, 2013].

This productivity increase has been attributed to an increased flux of organic matter to the seafloor and possible resulting drawdown of atmospheric CO_2 during the Mi-1 event [*Diester-Haass et al.*, 2011; *Mawbey and Lear*, 2013]. This is further supported by productivity being in phase with $\delta^{18}O$ (and, thus, ice volume) at ODP Site 929 and by the fact that organic carbon burial acted as a positive feedback as climate cooled [*Diester-Haass et al.,* 2011; *Mawbey and Lear*, 2013]. The thick Mi-1 interval in Hole 516F is also characterized by a decrease in warm-water calcareous nannofossil and planktonic foraminiferal taxa and is interpreted as a shift to cooler surface waters (Figure 9). This would be expected during the transient

Table 2. Magnetic Polarity Reversals in Hole 516F

Chron	Base age (Ma)	Base depth (m bsf)	Top Age (Ma)	Top Depth (m bsf)
C6Bn.2n	22.268	196.26	—	—
C6Br	22.564	200.18	22.268	196.26
C6Cn.1n	22.754	204.86	22.564	200.18
C6Cn.1r	22.902	207.25	22.754	204.86
C6Cn.2n	23.030	215.78	22.902	207.25
C6Cn.2r	—	—	23.030	215.78
C6Cr	23.962	250.22	—	—
C7n.1n	—	—	23.962	250.22
C7n.2n	24.474	257.63	—	—
C7r	—	—	24.474	257.63

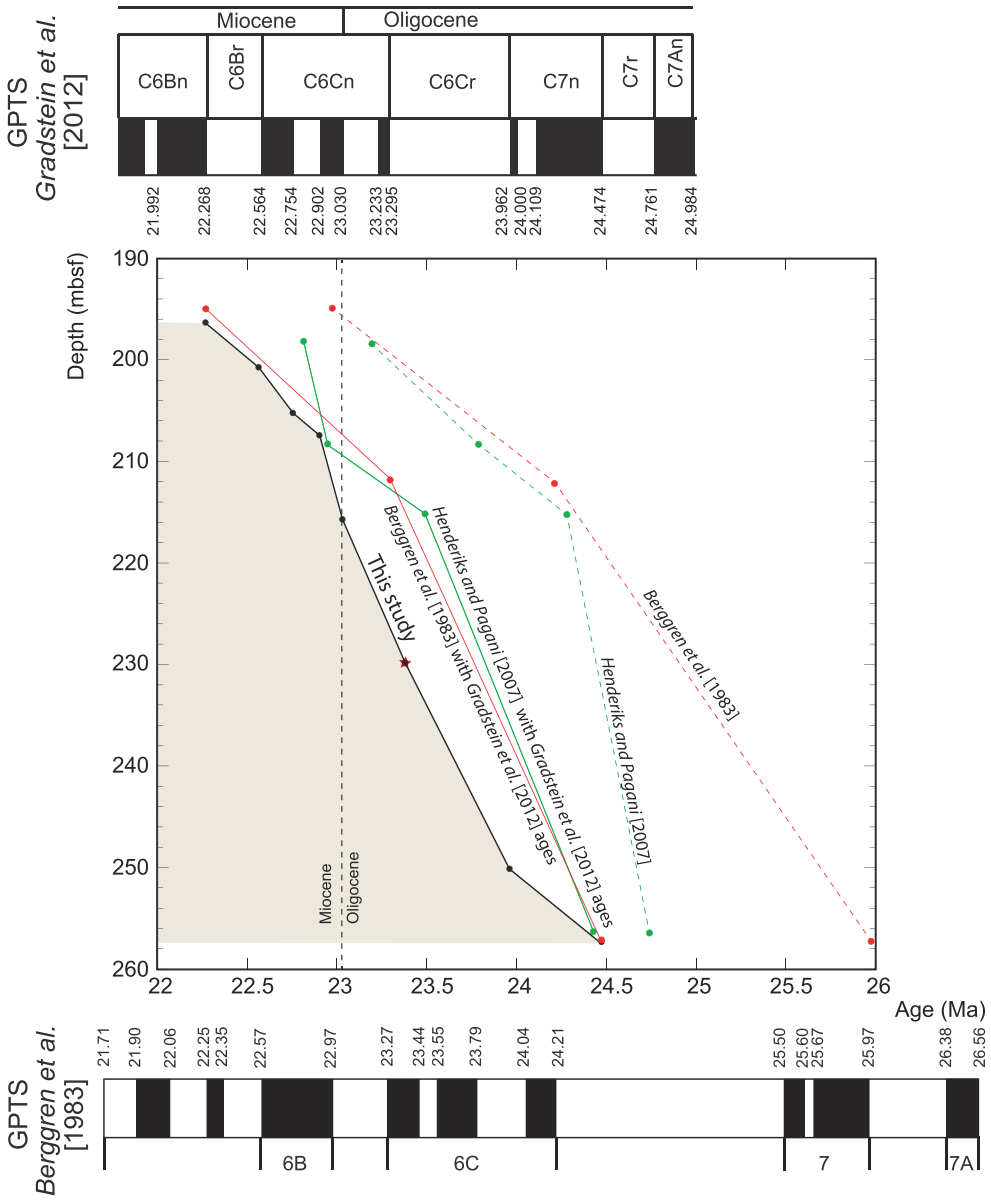

Figure 10. Age versus depth plot on the GPTS of *Gradstein et al.* [2012] (this study; black line), compared with the magnetic polarity record of *Berggren et al.* [1983] (red line). The latter authors used the GPTS of *Berggren et al.* [1985] (red dashed line). We also show the record of *Berggren et al.* [1983] with ages transferred to the GPTS of *Gradstein et al.* [2012] (red line). The age versus depth plot indicated in dashed green is derived from *Henderiks and Pagani* [2007]. We also show the record derived from *Henderiks and Pagani* [2007] with ages transferred to the GPTS of *Gradstein et al.* [2012] (green line). The age from the LO of *S. delphix* (mean depth of 229.8 m bsf) is indicated by a red star.

cooling event. If zonal winds were enhanced by glacial conditions during the Mi-1 event to force subantarctic surface waters further north to mix with subtropical surface waters (Figure 1), then conditions would have further favored planktonic productivity. Modern and last glacial observations [e.g., *Murphy et al.*, 2001; *Carter and Manighetti*, 2006] indicate that mixing of macronutrient-bearing but micronutrient-limited subantarctic surface waters with micronutrient-bearing subtropical waters enhances nannoplankton and foraminiferal production, which depend on insolation, water temperature, upper ocean thermal structure, and nutrient availability. Attribution of the productivity increase to a change in upper ocean water masses and frontal position is consistent with the presence of the apparently redeposited volcanic clasts (section 6.1), the majority of which occur within the Mi-1 event, which could mark a local response to the change in current

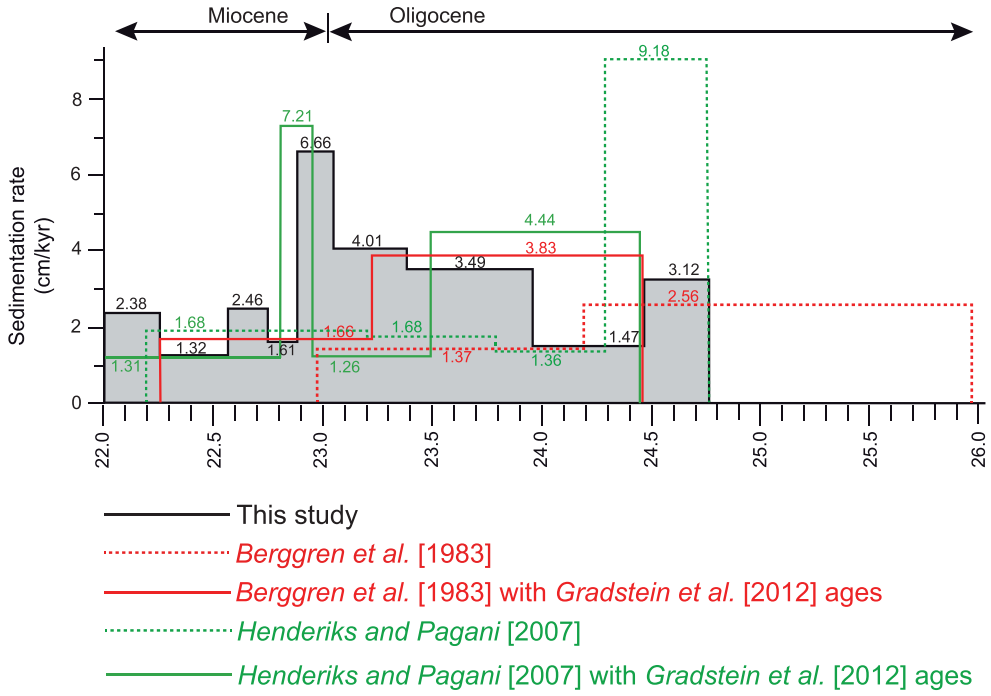

Figure 11. Sedimentation rates at DSDP Site 516F calculated for our new age model (black line). This record is compared with sedimentation rates from *Berggren et al.* [1983] with the GPTS of *Berggren et al.* [1985] (dashed red line), and with sedimentation rates calculated using *Berggren et al.* [1983] but with ages transferred to the GPTS of *Gradstein et al.* [2012] (red line). The sedimentation rates indicated in dashed green are derived from *Henderiks and Pagani* [2007]. The sedimentation rates derived from *Henderiks and Pagani* [2007] but with ages transferred to the GPTS of *Gradstein et al.* [2012] are indicated in green.

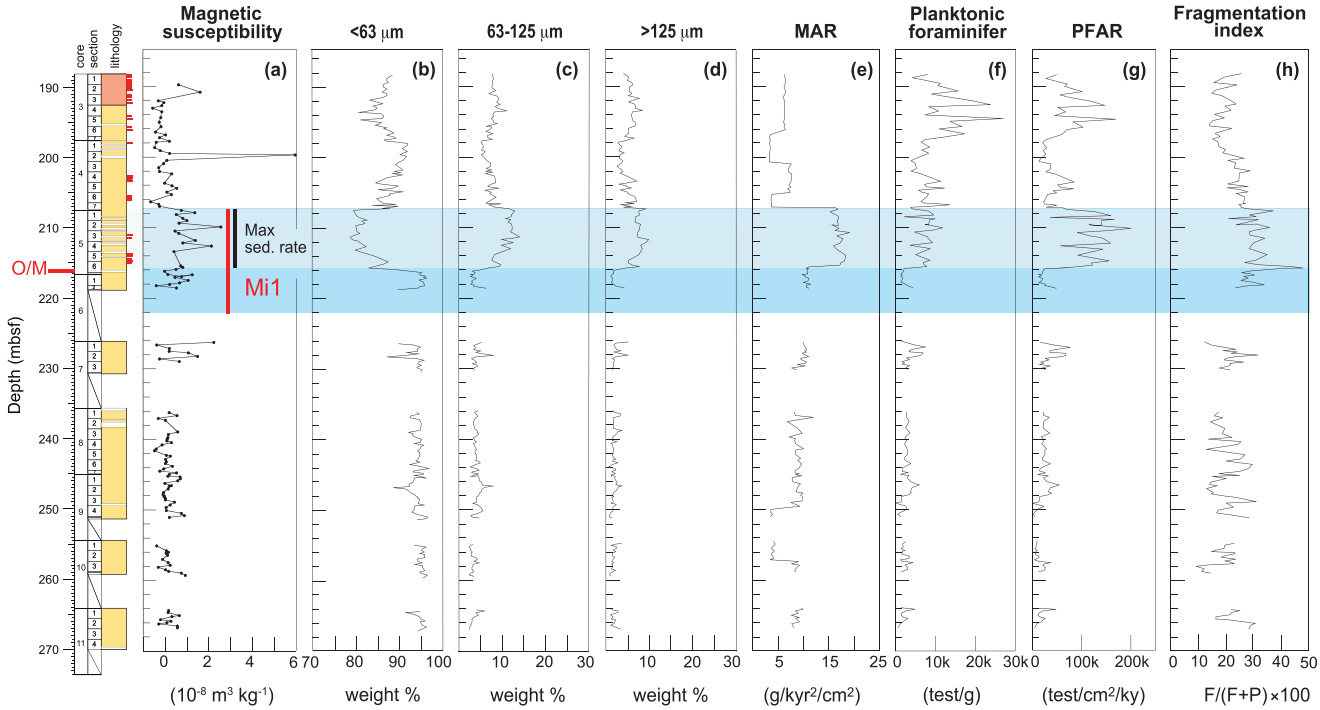

Figure 12. Stratigraphic plot of (a) κ, the percentages of the (b) <63 μm, (c) 63–125 μm, and (d) >125 μm sediment fractions, (e) MAR, (f) planktonic foraminiferal tests per gram of sediment, (g) planktonic foraminifer accumulation rate (PFAR), and (h) planktonic foraminiferal fragmentation index (FI). In the interval with the highest sedimentation rate, there is an increase in the 63–125 and >125 μm washed fractions. The PFAR trend reflects the increase in sedimentation rate from around 250 m bsf and culminates at the peaks of the early Miocene (Mi-1 and Mi-1.1) glacial events.

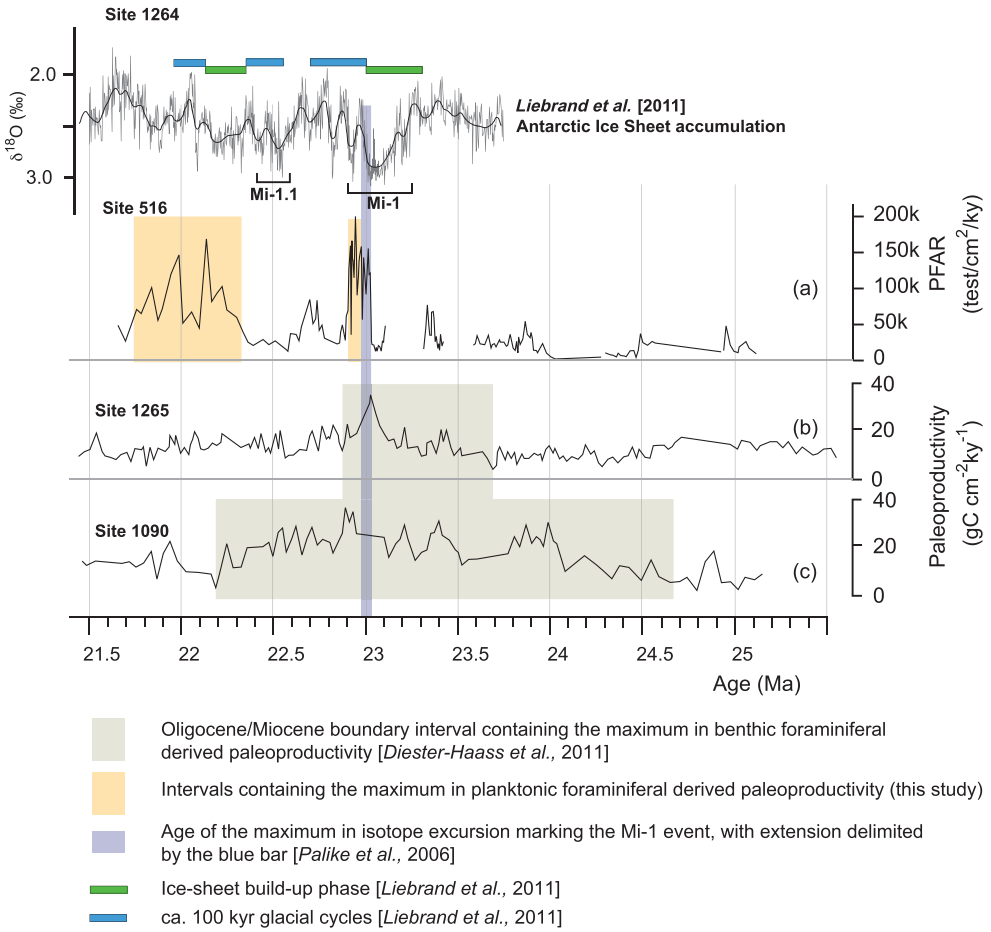

Figure 13. Comparison of (a) the DSDP Site 516F PFAR index profile compared to paleoproductivity records from (b) ODP 1265 (Walvis Ridge; 29°S, 3°E) and (c) 1090 (Aguhlas Ridge; 43°S, 30°W) [*Diester-Haass et al.*, 2011]. The top panel of Figure 13a contains the δ^{18}O record from Site 1264 [*Liebrand et al.*, 2011] including a Gaussian-weighted moving average (100 kyr) of the δ^{18}O record.

regime. The main sustained zone of elevated susceptibility in our record (corresponding to increased clast redeposition) is contemporaneous with a prominent peak in sortable silt mean diameter (a proxy for current velocity) reported by *Pfuhl and McCave* [2005] at ODP Site 1172 in the southwestern Tasman Sea, which suggests that the current shifts inferred from our record were driven by a hemispheric-scale process. Further corroboration is provided by *Liebrand et al.* [2011] who documented δ^{18}O gradients between Atlantic sites at different latitudes: they report an event at 22.9 Ma (again, coincident with elevated redeposition at DSDP-516F) during which intersite δ^{18}O gradients disappeared, indicating a major ocean current reorganization. Coarsening of Mi-1 sediments (e.g., the 81 μm peak in sample 5-2-88, Figure 6) is likely to reflect a change in carbonate production, with colder Mi-1 surface waters enhancing foraminiferal production, although nannofossils remained dominant [*Barker et al.*, 1983]. In the highest sedimentation rate interval, the relative contribution of the 63–125 μm and >125 μm fractions increased (Figure 12), which reinforces the interpretation that the increased sedimentation rate and coarse fraction during the Mi-1 event were due to increased productivity. These results contrast with the suggestion of less intense southwestern Atlantic circulation before the late Miocene [*Dalziel et al.*, 2013], with minimal bottom water formation associated with a weak and simple N-S overturning circulation.

Increased foraminiferal fragmentation also occurred during the Mi-1 event, probably due to increased bottom water corrosiveness during Mi-1 at this intermediate water depth site [e.g., *Stuut et al.*, 2002]. This would be consistent with strengthening of a proto Upper Circumpolar Deep Water during Mi-1, which could also have contributed to increased bottom water corrosiveness at Site 516.

7. Conclusions

We have produced a revised age model for Oligocene-Miocene sediments from DSDP Hole 516F, a key South Atlantic stratigraphic reference section [*Berggren et al.*, 1983; *Pujol*, 1983; *Spezzaferri*, 1994]. We define a more detailed succession of geomagnetic reversals across the Oligocene-Miocene boundary, including more accurate constraints on the base of subchron C6Cn.2n, which formally defines the base of the Neogene [*Steininger et al.*, 1997]. Even when the *Berggren et al.* [1983] and *Henderiks and Pagani* [2007] age control points are transposed onto the *Gradstein et al.* [2012] time scale, our refined chronology is significantly different in terms of both ages and sedimentation rates compared with the previous age model: the offset from the *Henderiks and Pagani* [2007] ages peaks at around 470 kyr. The new ages are systematically younger than those previously determined (Figures 9 and 10).

With the new age model, we observe a progressive sedimentation rate increase from 24.5 Ma to 22.9 Ma, with the highest rate coincident with the Mi-1 glacial event. This increase is ascribed to increased productivity and organic carbon burial and has been observed at other coeval deep water sites. We document a progressive increase in areal extent of carbon burial leading up to the Mi-1 event, starting with the Southern Ocean and extending to midlatitudes in the South Atlantic basin. This carbon burial would have resulted in drawdown of atmospheric CO_2 and provided a trigger for the Mi-1 cooling. The gradual increase in carbon burial extent also suggests that a tipping point was reached in the carbon cycle, resulting in the Mi-1 event. In addition, productivity and sedimentation rates decreased abruptly as deglaciation commenced after Mi-1, which supports the notion that decreased carbon burial could have been the causal mechanism for deglaciation after Mi-1. An additional elevation in sedimentation rate at ~24.5 Ma correlates with the δ^{18}O Oi2D glacial event and further supports the idea that carbon cycling had a major influence on these climate changes. The elevated sedimentation rate, along with an increased coarse sediment fraction, can be attributed to a glacially induced ocean current shift. A reorganization of water masses caused the incursion of redeposited clasts and increased the foraminiferal fragmentation index in the Mi-1 interval. Our age model will affect the inferred ages of several bioevents across the Oligocene-Miocene boundary for which Hole 516F has been used as a reference section [e.g., *Berggren et al.*, 1983, 1985, 1995; *Spezzaferri*, 1994]. As investigations continue into the triggers and mechanisms of the Mi-1 event, development of accurate chronologies will become increasingly important in correlating disparate records and establishing cause-and-effect relationships. Our work also demonstrates the potential for obtaining valuable new results when key sites from previous decades are reinvestigated using modern techniques [e.g., *Roberts et al.*, 2003a; *Florindo and Roberts*, 2005; *Florindo et al.*, 2013].

Acknowledgments
We thank the IODP for granting permission to work on the studied cores, and IODP personnel at the Bremen Core Repository and Christian Ohneiser for their assistance with sampling. The IODP is sponsored by the U.S. National Science Foundation (NSF) and participating countries under management of Joint Oceanographic Institutions (JOI), Inc. IODP is supported by NSF, Japan's MEXT, ECORD, and the People's Republic of China Ministry of Science and Technology. We thank Christian Ohneiser for assistance with sampling, Diederik Liebrand for providing the δ^{18}O data set from ODP Site 1264 (Walvis Ridge), plotted in Figure 13, Giovanna Gianelli for sample preparation and granulometric analysis and Massimo Mari for manufacturing the custom-made plexiglas sample holder. We are grateful to two anonymous reviewers for constructive review comments and Heiko Pälike for efficient editorial handling. This contribution is dedicated to the memory of our colleague Peter F. Barker, Co-Chief Scientist of DSDP Leg 72. Data presented in this paper are available by contacting the corresponding author (fabio.florindo@ingv.it).

References

Backman, J., I. Raffi, D. Rio, E. Fornaciari, and H. Pälike (2012), Biozonation and biochronology of Miocene through Pleistocene calcareous nannofossils from low and middle latitudes, *Newsl. Stratigr.*, *45*, 221–244.

Barker, P. F. (1983), Tectonic evolution and subsidence history of the Rio Grande Rise, in *Init. Rep. DSDP, 72*, edited by P. F. Barker, et al., pp. 953–976, U.S. Govt. Printing Office, Washington, D.C., doi:10.2973/dsdp.proc.72.151.1983.

Barker, P. F., et al. (1981), Deep Sea Drilling Project Leg 72: Southwest Atlantic paleocirculation and Rio Grande Rise tectonics, *Geol. Soc. Am. Bull.*, *92*, 294–309.

Barker, P. F., et al. (1983), Site 516: Rio Grande Rise, in *Init. Rep. DSDP, 72*, edited by P. F. Barker, et al., pp. 155–338, U.S. Govt. Printing Office, Washington, D.C., doi:10.2973/dsdp.proc.72.105.1983.

Barker, P. F., G. M. Filippelli, F. Florindo, E. Martin, and H. D. Scher (2007), Onset and role of the Antarctic Circumpolar Current, *Deep Sea Res., Part II*, *54*, 2388–2398.

Bé, A. W. H., D. A. Caron, and O. R. Anderson (1981), Effects on feeding frequency on life processes of the planktonic foraminifer *Globigerinoides sacculifer* in laboratory culture, *J. Mar. Biol. Assoc. UK*, *61*, 257–277.

Berger, W. H. (1970), Planktonic foraminifera: Selective solution and the lysocline, *Mar. Geol.*, *8*, 111–138.

Berggren, W. A., M. P. Aubry, and N. Hamilton (1983), Neogene magnetobiostratigraphy of Deep Sea Drilling Project Site 516 (Rio Grande Rise, South Atlantic), in *Init. Rep. DSDP, 72*, edited by P. F. Barker, et al., pp. 675–714, U.S. Govt. Print. Off., Washington, D. C., doi:10.2973/dsdp.proc.72.130.1983.

Berggren, W. A., D. V. Kent, and J. A. Van Couvering (1985), Neogene geochronology and chronostratigraphy, in *The Chronology of the Geological Record*, *Geol. Soc. Lond. Mem.*, vol. 10, edited by N. J. Snelling, pp. 211–260.

Berggren, W. A., D. V. Kent, C. C. Swisher III, and M.-P. Aubry (1995), A revised Cenozoic geochronology and chronostratigraphy, in *Geochronology, Time Scales and Global Stratigraphic Correlation: Framework for an Historical Geology*, *Soc. Econ. Paleontol. Mineral. Spec. Publ.*, vol. 54, edited by W. A. Berggren et al., pp. 129–212.

Billups, K., and D. P. Schrag (2002), Paleotemperatures and ice volume of the past 27 Myr revisited with paired Mg/Ca and $^{18}O/^{16}O$ measurements on benthic foraminifera, *Paleoceanography*, *17*(1), 1003, doi:10.1029/2000PA000567.

Billups, K., J. E. T. Channell, and J. Zachos (2002), Late Oligocene to early Miocene geochronology and paleoceanography from the subantarctic South Atlantic, *Paleoceanography*, *17*(1), 1004, doi:10.1029/2000PA000568.

Billups, K., H. Pälike, J. E. T. Channell, J. C. Zachos, and N. J. Shackleton (2004), Astronomic calibration of the late Oligocene through early Miocene geomagnetic polarity time scale, *Earth Planet. Sci. Lett.*, *224*, 33–44.
Blaj, T., J. Backman, and I. Raffi (2009), Late Eocene to Oligocene preservation history and biochronology of calcareous nannofossils from paleo-equatorial Pacific Ocean sediments, *Riv. Ital. Paleontol. Strat.*, *115*, 67–85.
Bloemendal, J., J. W. King, F. R. Hall, and S.-J. Doh (1992), Rock magnetism of late neogene and pleistocene deep-sea sediments: Relationship to sediment source, diagenetic processes, and sediment lithology, *J. Geophys. Res.*, *97*, doi:10.1029/91JB03068.
Boulila, S., B. Galbrun, K. G. Miller, S. F. Pekar, J. V. Browning, J. Laskar, and J. D. Wright (2011), On the origin of Cenozoic and Mesozoic "third-order" eustatic sequences, *Earth Sci. Rev.*, *109*, 94–112.
Bryan, W. B., and R. A. Duncan (1983), Age and provenance of clastic horizons from Hole 516F, in *Init. Rep. DSDP, 72*, edited by P. F. Barker, et al., pp. 475–477, U.S. Govt. Printing Office, Washington, D.C., doi:10.2973/dsdp.proc.72.118.1983.
Carter, L., and B. Manighetti (2006), Glacial/interglacial control of terrigenous and biogenic fluxes in the deep ocean off a high input, collisional margin: A 139 kyr-record from New Zealand, *Mar. Geol.*, *226*, 307–322.
Channell, J. E. T., S. Galeotti, E. E. Martin, K. Billups, H. Scher, and J. S. Stoner (2003), Eocene to Miocene magnetic, bio- and chemo-stratigraphy at ODP site 1090 (subantarctic South Atlantic), *Geol. Soc. Am. Bull.*, *115*, 607–623.
Dalziel, I. W. D., L. A. Lawver, J. A. Pearce, P. F. Barker, A. R. Hastie, D. N. Barfod, H. W. Schenke, and M. B. Davis (2013), A potential barrier to deep Antarctic circumpolar flow until the late Miocene?, *Geology*, *41*, 947–950, doi:10.1130/G34352.1.
Diester-Haass, L., K. Billups, and K. Emeis (2011), Enhanced paleoproductivity across the Oligocene/Miocene Boundary as evidenced by benthic foraminiferal accumulation rates, *Palaeogeogr. Palaeoclimatol. Palaeoecol.*, *302*, 464–473.
Florindo, F., and A. P. Roberts (2005), Eocene-Oligocene magnetobiostratigraphy of ODP sites 689 and 690, Maud Rise, Weddell Sea, Antarctica, *Geol. Soc. Am. Bull.*, *117*, 46–66.
Florindo, F., R. K. Farmer, D. M. Harwood, R. D. Cody, R. Levy, S. M. Bohaty, L. Carter, and A. Winkler (2013), Palaeomagnetism of sediments from Southern Ocean ODP Site 744 (southern Kerguelen Plateau): Implications for early-to-middle Miocene climate in Antarctica, *Global Planet. Change*, *110*, 434–454, doi:10.1016/j.gloplacha.2013.05.004.
Gennari, R., D. Persico, F. Florindo, E. Turco, and G. Villa (2014), Integrated magnetobiostratigraphy at the Oligocene/Miocene transition in the southwestern Atlantic Ocean (DSDP Leg 72, Hole 516F), 11th EGU General Assembly 2014, *Geophys. Res. Abstr.*, *16*, EGU2014–11688.
Gradstein, F. M., J. G. Ogg, M. D. Schmitz, and G. M. Ogg (2012), *The Geologic Time Scale 2012*, pp. 1144, Elsevier, Oxford.
Hamilton, L. J. (2006), Structure of the Subtropical Front in the Tasman Sea, *Deep Sea Res., Part I*, *53*, 1989–2009.
Harrison, R. J., and J. M. Feinberg (2008), FORCinel: An improved algorithm for calculating first-order reversal curve distributions using locally weighted regression smoothing, *Geochem. Geophys. Geosyst.*, *9*, Q05016, doi:10.1029/2008GC001987.
Henderiks, J., and M. Pagani (2007), Refining ancient carbon dioxide estimates: Significance of coccolithophore cell size for alkenone-based pCO_2 records, *Paleoceanography*, *22*, PA3202, doi:10.1029/2006PA001399.
Heslop, D., and A. P. Roberts (2012), Estimation of significance levels and confidence intervals for first-order reversal curve distributions, *Geochem. Geophys. Geosyst.*, *13*, Q12Z40, doi:10.1029/2012GC004115.
Hess, J., M. L. Bender, and J.-G. Schilling (1986), Evolution of the ratio of strontium-87 to strontium-86 in seawater from Cretaceous to Present, *Science*, *231*, 979–984.
Hrouda, F. (1994), A technique for the measurement of thermal changes of magnetic susceptibility of weakly magnetic rocks by the CS-2 apparatus and KLY-2 Kappabridge, *Geophys. J. Int.*, *118*, 604–612.
Johnson, D. A. (1983), Regional oceanographic setting of the southwestern Atlantic, in *Init. Rep. DSDP, 72*, edited by P. F. Barker, et al., pp. 15–35, U.S. Govt. Printing Office, Washington, D.C., doi:10.2973/dsdp.proc.72.102.1983.
Kirschvink, J. L. (1980), The least-squares line and plane and the analysis of palaeomagnetic data, *Geophys. J. R. Astron. Soc.*, *62*, 699–718.
Koltermann, K. P., V. V. Gouretski, and K. Jancke (2011), Hydrographic Atlas of the World Ocean Circulation Experiment (WOCE), in *Volume 3: Atlantic Ocean*, edited by M. Sparrow, P. Chapman, and J. Gould, International WOCE Project Office, Southampton, U. K.
Kucera, M. (2007), Planktonic foraminifera as tracers of past oceanic environments, in *Proxies in Late Cenozoic Paleoceanography: Pt. 2: Biological Tracers and Biomarkers*, edited by C. Hillaire-Marcel and A. de Vernal, pp. 213–262, Elsevier.
Larqué, L., K. Maamaatuaiahutapu, and V. Garçon (1997), On the intermediate and deep water flows in the South Atlantic Ocean, *J. Geophys. Res.*, *102*, 12,425–12,440, doi:10.1029/97JC00629.
Liebrand, D., L. J. Lourens, D. A. Hodell, B. de Boer, R. S. W. van de Wal, and H. Pälike (2011), Antarctic ice sheet and oceanographic response to eccentricity forcing during the early Miocene, *Clim. Past*, *7*, 869–880, doi:10.5194/cp-7-869-2011.
Lourens, L., F. Hilgen, N. J. Shackleton, J. Laskar, and D. Wilson (2004), The Neogene Period, in *A Geologic Time Scale 2004*, edited by F. M. Gradstein, J. G. Ogg, and A. Smith, pp. 409–440, Cambridge Univ. Press, Cambridge, U. K.
Lurcock, P. C., and G. S. Wilson (2012), PuffinPlot: A versatile, user-friendly program for paleomagnetic analysis, *Geochem. Geophys. Geosyst.*, *13*, Q06Z45, doi:10.1029/2012GC004098.
Lyle, M., S. Gibbs, T. C. Moore, and D. K. Rea (2007), Late Oligocene initiation of the Antarctic Circumpolar Current: Evidence from the South Pacific, *Geology*, *35*, 691–694, doi:10.1130/G23806A.1.
Maiorano, P., and S. Monechi (1998), Revised correlation of early and middle Miocene calcareous nannofossil events and magnetostratigraphy from DSDP Site 563 (North Atlantic Ocean), *Mar. Micropal.*, *35*, 235–255.
Mawbey, E. M., and C. H. Lear (2013), Carbon cycle feedbacks during the Oligocene-Miocene transient glaciation, *Geology*, *41*, 963–966, doi:10.1130/G34422.1.
Miller, K. G., M. D. Feigenson, D. V. Kent, and R. K. Olsson (1988), Upper Eocene to Oligocene isotope ($^{87}Sr/^{86}Sr$, $\delta^{18}O$, $\delta^{13}C$) standard section, Deep Sea Drilling Project Site 522, *Paleoceanography*, *3*, 223–233, doi:10.1029/PA003i002p00223.
Miller, K. G., J. D. Wright, and R. G. Fairbanks (1991), Unlocking the ice house: Oligocene-Miocene oxygen isotopes, eustasy, and margin erosion, *J. Geophys. Res.*, *96*, 6829–6848, doi:10.1029/90JB02015.
Mohriak, W. U., M. Nóbrega, M. E. Odegard, B. S. Gomes, and W. G. Dickson (2010), Geological and geophysical interpretation of the Rio Grande Rise, south-eastern Brazilian margin: Extensional tectonics and rifting of continental and oceanic crusts, *Petrol. Geosci.*, *16*, 231–245, doi:10.1144/1354-079309-910.
Mojtahid, M., et al. (2013), High resolution Holocene record in the southeastern Bay of Biscay: Global versus regional climate signals, *Palaeogeogr. Palaeoclimatol. Palaeoecol.*, *377*, 28–44.
Murphy, R. J., M. H. Pinkerton, K. M. Richardson, J. M. Bradford-Grieve, and P. W. Boyd (2001), Phytoplankton distributions around New Zealand derived from SeaWiFS remotely-sensed ocean colour data, *N.Z. J. Mar. Freshwater Res.*, *35*, 343–362, doi:10.1080/00288330.2001.9517005.
Murray, R. J., and C. J. C. Reason (1999), Influences of topography on the modeling of abyssal water masses. Part I: Effects of channel representation, *J. Phys. Oceanogr.*, *29*, 2851–2871, doi:10.1175/1520-0485(1999)029<2851:IOTOTM>2.0.CO;2.

Naish, T. R., et al. (2001), Orbitally induced oscillations in the East Antarctic ice sheet at the Oligocene/Miocene boundary, *Nature*, *413*, 719–723.
O'Connor, J. M., and R. A. Duncan (1990), Evolution of the Walvis Ridge-Rio Grande Rise hot spot system: Implications for African and South American plate motions over plumes, *J. Geophys. Res.*, *95*, 17,475–17,502, doi:10.1029/JB095iB11p17475.
Orsi, A. H., G. C. Johnson, and J. L. Bullister (1999), Circulation, mixing and production of Antarctic Bottom Water, *Progr. Oceanogr.*, *43*, 55–109.
Pagani, M., M. A. Arthur, and K. H. Freeman (2000), Variations in Miocene phytoplankton growth rates in the southwest Atlantic: Evidence for changes in ocean circulation, *Paleoceanography*, *15*, 486–496, doi:10.1029/1999PA000484.
Pagani, M., J. C. Zachos, K. H. Freeman, B. Tripple, and S. Bohaty (2005), Marked decline in atmospheric carbon dioxide concentrations during the Paleogene, *Science*, *309*, 600–603.
Paillard, D., L. Labeyrie, and P. Yiou (1996), Macintosh program performs time-series analysis, *Eos Trans. AGU*, *77*(39), 379–379, doi:10.1029/96EO00259.
Pälike, H., J. Frazier, and J. C. Zachos (2006), Extended orbitally forced paleoclimatic records from the equatorial Atlantic Ceara Rise, *Quat. Sci. Rev.*, *25*, 3138–3149, doi:10.1016/j.quascirev.2006.02.011.
Pekar, S. F., and R. DeConto (2006), High-resolution ice-volume estimates for the early Miocene: Evidence for a dynamic ice sheet in Antarctica, *Palaeogeogr. Palaeoclimatol. Palaeoecol.*, *231*, 101–109.
Pekar, S. F., N. Christie-Blick, M. A. Kominz, and K. G. Miller (2002), Calibration between eustatic estimates from backstripping and oxygen isotopic record for the Oligocene, *Geology*, *30*, 903–906.
Pekar, S. F., R. DeConto, and D. M. Harwood (2006), Resolving a late Oligocene conundrum: Deep-sea warming versus Antarctic glaciation, *Palaeogeogr. Palaeoclimatol. Palaeoecol.*, *231*, 29–40.
Petrova, G. N., T. B. Nechaeva, G. Z. Gurary, and V. A. Chmerev (1983), Ferromagnetic fraction of Cretaceous and Cenozoic sediments of the Rio Grande Rise and Brazil Basin, in *Init. Rep. DSDP, 72*, edited by P. F. Barker, pp. 591–598, et al., U.S. Govt. Printing Office, Washington, D. C., doi:10.2973/dsdp.proc.72.127.1983.
Pfuhl, H. A., and I. N. McCave (2005), Evidence for late Oligocene establishment of the Antarctic Circumpolar Current, *Earth Planet. Sci. Lett.*, *235*, 715–728.
Pike, C. R., A. P. Roberts, and K. L. Verosub (1999), Characterizing interactions in fine magnetic particle systems using first order reversal curves, *J. Appl. Phys.*, *85*, 6660–6667.
Pike, C. R., A. P. Roberts, and K. L. Verosub (2001), First-order reversal curve diagrams and thermal relaxation effects in magnetic particles, *Geophys. J. Int.*, *145*, 721–730.
Plancq, J., V. Grossi, J. Henderiks, L. Simon, and E. Mattioli (2012), Alkenone producers during late Oligocene–early Miocene revisited, *Paleoceanography*, *27*, PA1202, doi:10.1029/2011PA002164.
Plancq, J., E. Mattioli, J. Henderiks, and V. Grossi (2013), Global shifts in Noelaerhabdaceae assemblages during the late Oligocene–early Miocene, *Mar. Micropal.*, *103*, 40–50.
Pujol, C. (1983), Cenozoic planktonic foraminiferal biostratigraphy of the southwestern Atlantic (Rio Grande Rise, South Atlantic), in *Init. Rep. DSDP, 72*, P. F. Barker, et al., pp. 623–674, U.S. Govt. Printing Office, Washington, D. C., doi:10.2973/dsdp.proc.72.129.1983.
Reid, J. L., W. D. Nowlin, and W. C. Patzert (1977), On the characteristics and circulation of the southwestern Atlantic Ocean, *J. Phys. Oceanogr.*, *7*, 62–91.
Roberts, A. P., C. R. Pike, and K. L. Verosub (2000), First-order reversal curve diagrams: A new tool for characterizing the magnetic properties of natural samples, *J. Geophys. Res.*, *105*, 28,461–28,475, doi:10.1029/2000JB900326.
Roberts, A. P., S. J. Bicknell, J. Byatt, S. M. Bohaty, F. Florindo, and D. M. Harwood (2003a), Magnetostratigraphic calibration of Southern Ocean diatom datums from the Eocene-Oligocene of Kerguelen Plateau (Ocean Drilling Program sites 744 and 748), *Palaeogeogr. Palaeoclimatol. Palaeoecol.*, *198*, 145–168.
Roberts, A. P., G. S. Wilson, D. M. Harwood, and K. L. Verosub (2003b), Glaciation across the Oligocene-Miocene boundary in Southern McMurdo Sound, Antarctica: New chronology from the CIROS-1 drill hole, *Palaeogeogr. Palaeoclimatol. Palaeoecol.*, *198*, 113–130.
Roberts, A. P., D. Heslop, X. Zhao, and C. R. Pike (2014), Understanding fine magnetic particle systems through use of first-order reversal curve (FORC) diagrams, *Rev. Geophys.*, *52*, 557–602, doi:10.1002/2014RG000462.
Schettino, A., and C. R. Scotese (2001), New Internet software aids paleomagnetic analysis and plate tectonic reconstructions, *Eos Trans. AGU*, *82*(45), 530–536, doi:10.1029/01EO00316.
Schmid, C., G. Siedler, and W. Zenk (2000), Dynamics of intermediate water circulation in the subtropical South Atlantic, *J. Phys. Oceanogr.*, *30*, 3191–3211, doi:10.1175/1520-0485(2000)030<3191:DOIWCI>2.0.CO;2.
Schmitz, W. J., Jr. (1995), On the interbasin-scale thermohaline circulation, *Rev. Geophys.*, *33*, 151–173, doi:10.1029/95RG00879.
Shackleton, N. J., M. A. Hall, and E. Vincent (2000), Phase relationships between millennial scale events 64,000 to 24,000 years ago, *Paleoceanography*, *15*, 565–569, doi:10.1029/2000PA000513.
Shevenell, A. E., and J. P. Kennett (2007), Cenozoic Antarctic cryosphere evolution: Tales from deep-sea sedimentary records, *Deep Sea Res., Part II*, *54*, 2308–2324.
Spezzaferri, S. (1994), Planktonic foraminiferal biostratigraphy of the Oligocene and lower Miocene in the oceanic record. An overview, *Palaeontogr. Ital.*, *81*, 1–187.
Steininger, F. F., et al. (1997), The Global Stratotype Section and Point (GSSP) for the base of the Neogene, *Episodes*, *20*, 23–28.
Storti, F., and F. Balsamo (2010), Particle size distributions by laser diffraction: Sensitivity of granular matter strength to analytical operating procedures, *Solid Earth*, *1*, 25–48.
Stramma, L. (1989), The Brazil current transport south of 23°S, *Deep Sea Res., Part I*, *36*, 639–646.
Stramma, L., and M. England (1999), On the water masses and mean circulation of the South Atlantic Ocean, *J. Geophys. Res.*, *104*, 20,863–20,883, doi:10.1029/1999JC900139.
Stuut, J.-B. W., M. A. Prins, and J. H. F. Jansen (2002), Fast reconnaissance of carbonate dissolution based on the size distribution of calcareous ooze on Walvis Ridge, SE Atlantic Ocean, *Mar. Geol.*, *190*, 581–589.
Villa, G., and D. Persico (2006), Late Oligocene climatic changes: Evidence from calcareous nannofossils at Kerguelen Plateau Site 748 (Southern Ocean), *Palaeogeogr. Palaeoclimatol. Palaeoecol.*, *231*, 110–119, doi:10.1016/j.palaeo.2005.07.028.
Wang, X., R. Løvlie, X. Zhao, Z. Yang, F. Jiang, and S. Wang (2010), Quantifying ultrafine pedogenic magnetic particles in Chinese loess by monitoring viscous decay of superparamagnetism, *Geochem. Geophys. Geosyst.*, *11*, Q10008, doi:10.1029/2010GC003194.
Watkins, J. M., A. C. Mix, and J. Wilson (1998), Living planktic foraminifera in the central tropical Pacific Ocean: Articulating the equatorial "cold tongue" during La Niña, 1992, *Mar. Micropal.*, *33*, 157–174.
Wilson, G. S., S. F. Pekar, T. R. Naish, S. Passchier, and R. DeConto (2009), The Oligocene-Miocene boundary—Antarctic climate response to orbital forcing, in *Antarctic Climate Evolution: Developments in Earth & Environmental Sciences*, vol. 8, edited by F. Florindo and M. Seigert, pp. 369–400, Elsevier, Netherlands.

Woodruff, F., and S. M. Savin (1989), Miocene deep water oceanography, *Paleoceanography*, *4*, 87–140, doi:10.1029/PA004i001p00087.
Wright, J. D., K. G. Miller, and R. G. Fairbanks (1991), Evolution of modern deepwater circulation: Evidence from the late Miocene Southern Ocean, *Paleoceanography*, *6*, 275–290, doi:10.1029/90PA02498.
Zachos, J. C., W. A. Berggren, M. P. Aubry, and A. Mackensen (1992), Isotope and trace element geochemistry of Eocene and Oligocene foraminifers from Site 748, Kerguelen Plateau, in *Proc. ODP, Sci. Res.*, vol. 120, edited by R. Schlich et al., pp. 839–854, Ocean Drilling Program, College Station, Tex.
Zachos, J. C., M. Pagani, L. Sloan, E. Thomas, and K. Billups (2001a), Trends, rhythms and aberrations in global climate 65 Ma to present, *Science*, *292*, 686–693.
Zachos, J. C., N. J. Shackleton, J. Revenaugh, H. Pälike, and B. P. Flower (2001b), Climate response to orbital forcing across the Oligocene-Miocene boundary, *Science*, *292*, 274–278.
Zijderveld, J. D. A. (1967), A. C. demagnetization of rocks: Analysis of results, in *Methods in Palaeomagnetism*, *Dev. in Solid Earth Geophys.*, edited by D. W. Collinson, K. M. Creer, and S. K. Runcorn, pp. 254–286, Elsevier, Amsterdam.